Interplay of B-Site Off-Centering and Molecular Orientations in the Mixed Hybrid Perovskite $MAGe_{1-x}Sn_xI_3$

Erik Fransson,[†] Apinya Ngoipala,[†] Oskar Öjstedt,[‡] Maths Karlsson,[‡] Paul Erhart,[†] and Julia Wiktor*[,†]

†*Department of Physics and Astronomy, Chalmers University of Technology, SE-412 96 Gothenburg, Sweden*

‡*Department of Chemistry and Chemical Engineering, Chalmers University of Technology, SE-412 96 Gothenburg, Sweden*

E-mail: julia.wiktor@chalmers.se

Abstract

B-site mixing is a common strategy for tuning properties of halide perovskites. In the lead-free system $MAGe_{1-x}Sn_xI_3$, it brings tilting and off-centering into competition. Using large-scale molecular dynamics driven by a machine-learned interatomic potential, we map the structural behavior across the full composition range. $MAGeI_3$ exhibits strong polar B-site off-centering that remains nearly constant up to the cubic transition, together with methylammonium (MA) orientational order that weakens progressively on heating. By contrast, $MASnI_3$ combines octahedral tilting with weaker, predominantly antipolar off-centering. Ge-like behavior persists upon alloying and gives way to Sn-like behavior only beyond roughly 65 % Sn. In the high-temperature phases, the B-site cations remain locally off-centered but directionally disordered. On the Ge-rich side, the distorted inorganic framework biases the soft MA orientational landscape toward a restricted set of preferred directions. This coupling shows how the composition of the inorganic sublattice can tune molecular ordering in lead-free hybrid perovskites.

TOC Graphic

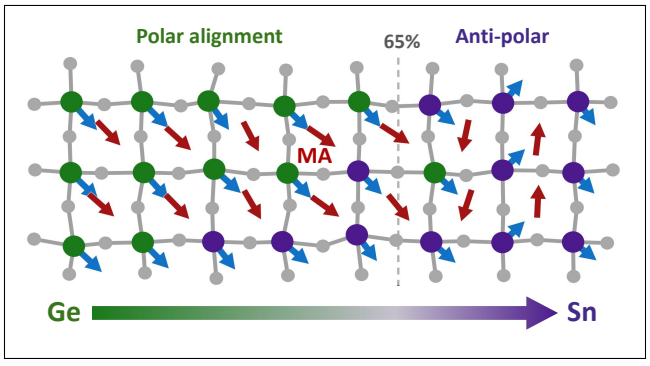

Halide perovskites, including the prototypical $MAPbI_3$, have emerged as one of the most promising classes of materials for photovoltaic applications, with lead-based perovskite solar cells now reaching power conversion efficiencies exceeding 26 %.[1] Despite the remarkable progress, the toxicity of lead remains a concern, motivating the exploration of alternative B-site cations such as Sn^{2+} and Ge^{2+}.[2–6] Sn-based compounds are currently the leading lead-free absorbers,[2–4,7] and partial substitution of Sn by Ge has been reported to improve the oxidation resistance and device performance of several Sn-based compositions and film architectures.[8–11] Beyond this practical appeal, the substitution of Pb by the lighter group-14 elements introduces qualitatively different structural chemistry that is of fundamental interest in its own right.[12–14]

Mixing on the B-site is a well-established strategy for continuously tuning the structural, electronic, and optical properties of halide perovskites.[15–18] Ge–Sn alloying is a particularly interesting case, since the two end members favor fundamentally different distortion mechanisms, which mixing brings into competition. In $MAGeI_3$, the small ionic radius of Ge^{2+} and its stereochemically active lone pair drive a pronounced polar off-centering of the B-site cation within the octahedral cage.[6,12,13] $MASnI_3$, by contrast, exhibits cooperative octahedral tilting instabilities, as does its Pb analog,[19–21] although weaker, antipolar off-centering tendencies of the Sn cation have been reported in the related compound $CsSnBr_3$.[22,23] These distortions have direct optoelectronic consequences: the photoluminescence intensity of $MAGeI_3$ is maximized at an intermediate degree of off-centering, peaking under pressure at a bond-length distortion of $\mathcal{D} \approx 0.2$ compared with $\mathcal{D} = 0.32$ at ambient conditions,[24] and the structural transitions of $MASnI_3$ are accompanied by pronounced changes in carrier lifetime and defect-related recombination.[25] The same lone-pair displacement makes the $CsGeX_3$ (X = Cl, Br, I) perovskites ferroelectric,[26,27] and $MAGeI_3$ is predicted to be comparably polar.[28] The mixed $MAGe_{1-x}Sn_xI_3$ system thus presents a setting in which polar off-centering, antipolar tendencies, octahedral tilting, and the molecular degrees of freedom coexist and compete. A previous first-principles study examined the mechanical and optoelectronic properties of

selected $MAGe_{1-x}Sn_xI_3$ compositions in an assumed orthorhombic structure,[29] and samples spanning the full composition range have been characterized experimentally at room temperature by X-ray diffraction and optical absorption, with the optical gap increasing from 1.3 eV at the Sn end to 2.0 eV at the Ge end.[30] The finite-temperature structural phase behavior of this system has, however, not been mapped. In particular, little is known about how the organic MA sublattice responds to and interacts with the competing inorganic distortions.

The MA molecule carries a permanent dipole moment, and its orientational energy landscape is shaped by electrostatic, hydrogen-bonding, steric, and lattice-mediated interactions with the inorganic cage.[31–33] In $MAGeI_3$, the strong $\langle 111 \rangle$ Ge off-centering may therefore lift the near-degeneracy of several local MA orientational minima and favor a restricted subset of preferred crystallographic directions. This behavior would contrast with $MAPbI_3$, in which the MA cations dynamically sample several symmetry-equivalent preferred orientations and reorient on picosecond timescales at ambient conditions,[34–42] and with $MASnI_3$ and $MASnBr_3$, for which orientational disorder persists to comparatively low temperatures.[43–45] Such polar molecular order would also be of interest for second-order nonlinear optics, since $MAGeI_3$ exhibits a strong, phase-matchable second-harmonic-generation response.[6] The nonlinear optical response is present in other Ge halide perovskites, both organic and inorganic, and has been shown to correlate with organic-cation ordering, chemical substitution, and framework distortion.[32,46–48] How the molecular orientational landscape evolves with composition and temperature, and whether molecular disorder feeds back on the stability of the inorganic polar order, remain unknown.

Here, we study the structural phase behavior of $MAGe_{1-x}Sn_xI_3$ across the full composition range using large-scale molecular dynamics (MD) simulations enabled by a machine-learned interatomic potential (MLIP).[49–51] We find that the two end members order in fundamentally different ways: $MAGeI_3$ develops strong long-range polar off-centering accompanied by MA orientational order with a much more gradual temperature dependence, whereas $MASnI_3$ combines octahedral tilting with weaker, predominantly antipolar off-centering. The Ge-

like behavior proves remarkably persistent upon alloying, dominating the phase diagram up to a crossover at roughly 65 % Sn. Above the respective ordering transitions, the B-site cations of all compositions remain locally off-centered while losing their directional order, entering a dynamically disordered state that parallels the local off-centering observed by pair-distribution-function analysis in the cubic phases of Sn- and Pb-based perovskites.[23,52,53] Our results show that the MA orientations follow the B-site off-centering pattern across the full composition range and establish B-site mixing as a handle on the interplay of off-centering, tilting, and molecular order in this lead-free system.

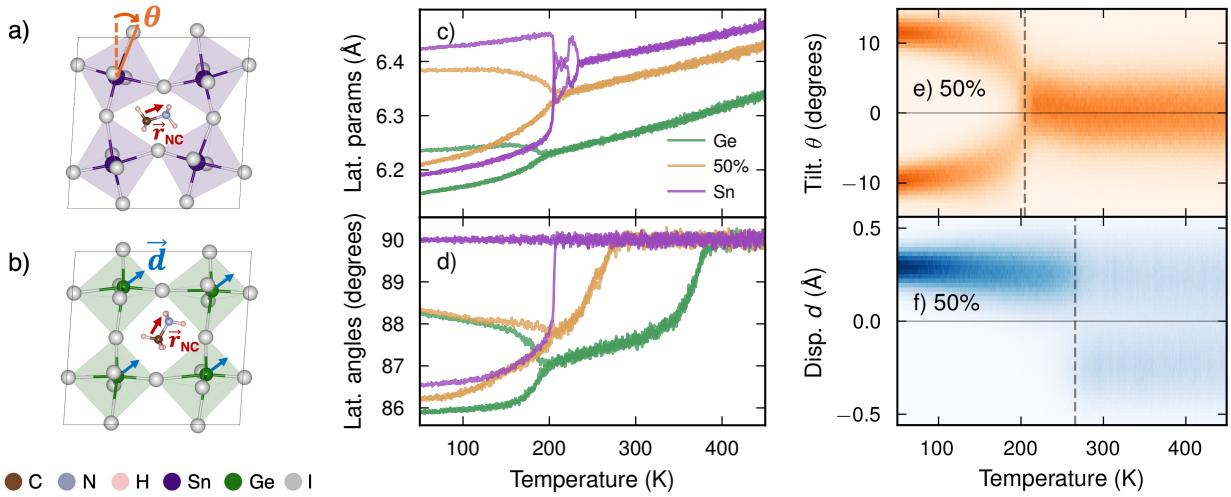

Figure 1: Atomistic structures of a) $MASnI_3$ and b) $MAGeI_3$, where the octahedral tilt angle (θ) and the off-centering displacement ($\boldsymbol{d}$) are indicated by orange and blue arrows, respectively. c) Lattice parameters and d) angles between the cell vectors along the heating runs of the Ge, the 50 % mixed, and the Sn systems. The lattice parameters are computed as the lengths of the cell vectors of a supercell based on the conventional cubic cell, and the lattice angles correspond to the angles between the cell vectors. e, f) Distributions of e) the tilt angles (θ) and f) the off-centering displacements (d), as indicated in a, b), along the heating run of the 50 % mixed system. The vertical dashed lines indicate the two phase transitions of the 50 % mixed system.

We determined the ground-state structures of the end members $MAGeI_3$ and $MASnI_3$ using a random structure search with the charge-aware neuroevolution potential (qNEP), following the approach previously applied to hybrid halide perovskites in Refs. 41,54. For the Ge system we find a structure exhibiting off-centering along the $\langle 111 \rangle$ direction, combined

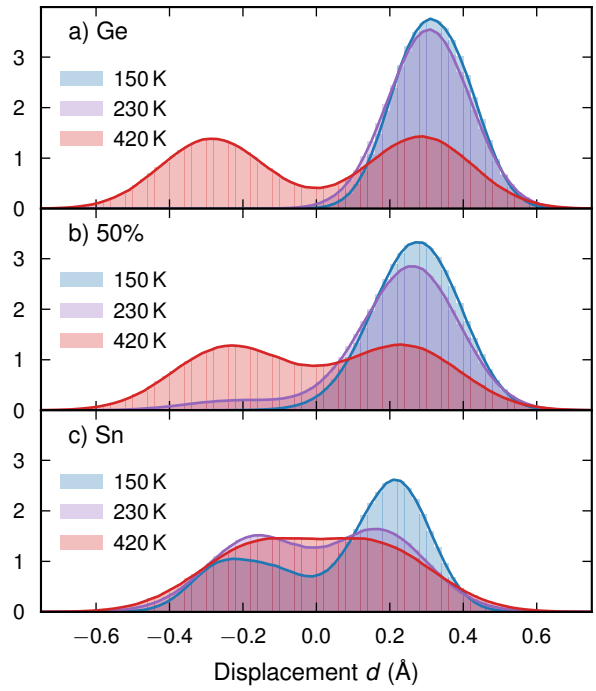

Figure 2: Distributions of the Cartesian components of the off-centering displacements $\boldsymbol{d}$, pooled over all B-site atoms, for a) Ge, b) the 50 % mixture, and c) Sn at 150 K, 230 K, and 420 K.

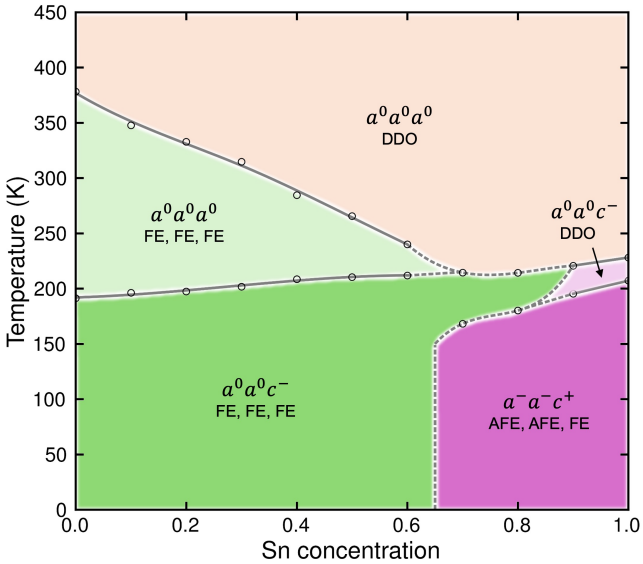

Figure 3: Predicted phase diagram of $MAGe_{1-x}Sn_xI_3$. Markers indicate points at which phase transitions are observed in the heating runs, and the lines serve as guides to the eye. Dashed lines correspond to regions of high uncertainty, where, for example, the exact phase was difficult to determine from the order parameters. The phases are labeled according to their off-centering order and octahedral tilt pattern.

with an out-of-phase tilt along one axis, as has also been found for $CsGeBr_3$.[55] For the Sn system we find a tilt pattern resembling the previously predicted *Pnma* ground state, namely $a^-a^-c^+$,[56] but with additional Sn off-centering resulting in a lower symmetry. The Sn off-centering is antiferroelectric (AFE), i.e., alternating between neighboring B sites, along two directions, and ferroelectric (FE) along the third direction, which coincides with the c^+ tilt axis. A closely related pattern has been reported for $CsSnBr_3$, where lone-pair-driven displacements are noncollinear within the plane normal to the unique octahedral tilt axis and ferroic along that axis,[22] in direct correspondence with the AFE/AFE/FE decomposition found here.

Because the optimal starting configuration for the mixed compositions is not known a priori, we initialized every composition from both end-member ground states and compared the energies obtained along the corresponding heating runs (Figure S6). The $MAGeI_3$ ground state yields the lower-energy starting point for Ge-rich compositions, whereas above roughly 65 % Sn the $MASnI_3$ ground state is preferred. While this criterion is admittedly crude, it provides the best available estimate of the appropriate starting structure for each composition.

First, we consider the phase transitions observed in the heating runs for the end members and the 50 % mixture (Figure 1). For $MAGeI_3$, two clear transitions are observed in the lattice parameters and the angles between the cell vectors (Figure 1c,d), at 200 K and around 380 K. These correspond to the system first losing its octahedral tilt (at 200 K) and subsequently losing the long-range order of the B-site off-centering displacements (at 380 K), as seen from the evolution of the order parameters (Figure S3). For $MASnI_3$ we also observe two transitions: a first one at 200 K, at which the long-range order of the Sn off-centering breaks down and the tilt pattern changes to $a^0a^0c^-$, followed closely by a second transition at around 230 K, at which the remaining tilt vanishes and the system adopts the high-symmetry cubic phase. The 50 % mixture follows the same transition sequence as the Ge end member, with transitions at 200 K and 280 K. The corresponding structural changes can be identified

from the distributions of the tilt angles and off-centering displacements (Figure 1e,f): the tilting vanishes at 200 K, and the long-range order of the off-centering is lost at 280 K.

A key difference between the Ge and Sn end members lies in the ordering of the B-site off-centering, with Ge exhibiting an FE distortion. The distributions of the Cartesian components of the displacements, pooled over all B-site atoms, are shown for three temperatures in Figure 2. For Ge, all displacements are aligned up to the transition to the cubic phase, giving rise to a single peak at a finite displacement. Above the transition, the distribution becomes a symmetric double Gaussian, showing that local off-centering persists while its long-range order is broken; direct visual inspection of the trajectories confirms repeated switching between the possible $\langle 111 \rangle$ states, a behavior we refer to as dynamically disordered off-centering (DDO).

The 50 % mixture shows very similar behavior, albeit with slightly smaller displacements. For Sn, the low-temperature distribution is asymmetric, reflecting the AFE/AFE/FE pattern of the ground state: the two AFE components contribute symmetrically about zero, while the FE component adds weight on one side only. In the intermediate phase, the long-range order is lost and the distribution becomes a symmetric double Gaussian, i.e., the Sn sublattice likewise enters a DDO state. At 420 K, the distribution appears unimodal and centered around zero, although local off-centering remains (Figure S5) and the distribution may equally well correspond to two strongly overlapping symmetric contributions. In either case, this indicates that the local off-centering in Sn becomes increasingly dynamic with increasing temperature. Altogether, this reflects the much stronger tendency toward off-centering in Ge than in Sn.

Experimentally, $MASnI_3$ is reported to undergo two transitions, at about 100 K and 275 K.[19,20] Our simulations likewise yield two transitions but compress them into a narrower window, at 200 K and 230 K. We note that the reported ambient-temperature structure, $P4mm$,[20] is polar rather than tilted, so that the experimental sequence may differ in character from the tilt-driven sequence found here.

The predicted structural parameters can be compared directly with experiment. At 300 K, $MAGeI_3$ is tilt-free and ferroelectrically ordered in our simulations, corresponding to an $R3m$-like structure, in agreement with the rhombohedral structure reported experimentally at ambient conditions.[6] We obtain a pseudocubic lattice parameter of 6.27 Å and a rhombohedral cell-angle deviation of 2.4°, close to the experimental values of 6.18 Å and 2.5°.[6] The Ge–I first coordination shell is split into bond lengths of 2.73 Å and 3.63 Å, compared with experimental values of 2.77 Å and 3.45 Å, respectively.[6,24] This corresponds to an off-centering distortion of $\mathcal{D} = 0.43$ (Figure S5), compared with $\mathcal{D} = 0.32$ from experiment.[24] Overall, the simulations reproduce the experimental symmetry, cell metric, and magnitude of the Ge off-centering distortion reasonably well.

For $MASnI_3$, the Sn–I first coordination shell at 360 K is clearly split, with a bond-length separation of 0.63 Å and an off-centering distortion of $\mathcal{D} = 0.29$ (Figure S5). This is consistent with pair-distribution-function measurements at the same temperature, which show a strongly distorted local Sn–I environment associated with $\langle 111 \rangle$ Sn off-centering, with a refined Sn displacement of approximately 0.22 Å.[52] In contrast, applying the same analysis to $MAPbI_3$ shows no resolved splitting of the Pb–I coordination shell, giving $\mathcal{D} = 0.0$, consistent with the very weak or absent local Pb off-centering found experimentally.[52] Together with $MAGeI_3$, these results reproduce the experimental trend from strong Ge off-centering, through substantial Sn off-centering, to very weak or absent off-centering in the Pb compound.

Lastly, we carry out order-parameter analysis, as described above, systematically across the composition range to map out the full phase diagram of the mixed system (Figure 3). The diagram reveals a crossover between Ge-like and Sn-like behavior at around 65 % Sn. On the Ge-rich side, the transition temperature to the cubic phase decreases almost linearly from 380 K to around 230 K with increasing Sn content. Near the crossover, compositions just above 65 % Sn pass through a Ge-like FE intermediate phase upon heating rather than the Sn-like $a^0a^0c^-$ phase. We note that the transitions in this composition and temperature region

are difficult to determine precisely (Figure S7–Figure S17). Uncertainties stemming from the underlying density-functional theory (DFT) reference data, finite MLIP accuracy, and finite-rate and hysteresis effects mean that the transition temperatures and phase boundaries should be regarded as qualitative and interpreted in the context of the present model and simulation protocol. The crossover composition of roughly 65 % Sn is likewise approximate, being resolved only to within the discrete set of compositions sampled here. Moreover, the phase diagram describes the structural behavior of the sampled disordered alloys and does not account for possible chemical ordering, miscibility, or competing phases beyond those considered here. What is clear, however, is the competition between the FE off-centering on the Ge-rich side and the AFE tendencies and octahedral tilting on the Sn-rich side, which gives rise to the rich phase behavior of this mixed system.

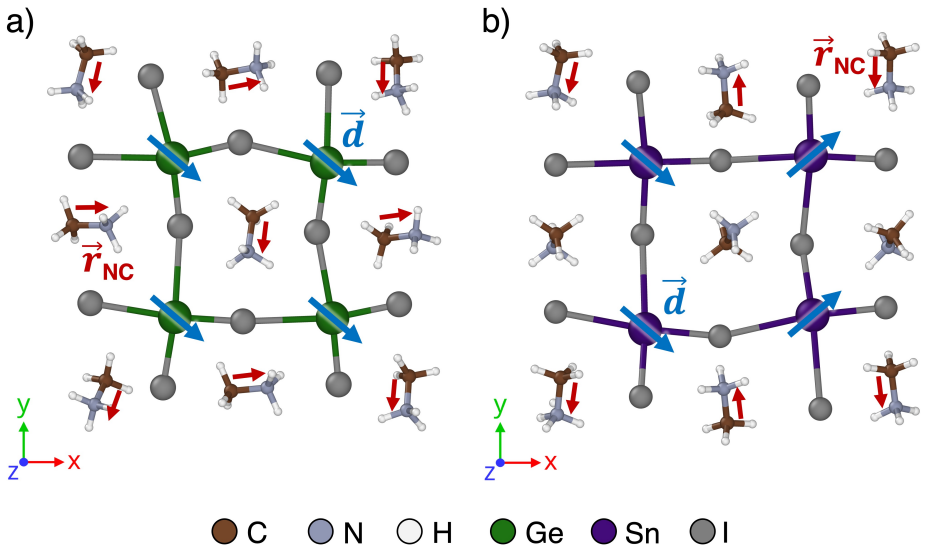

Figure 4: MD snapshots at 150 K for a) $MAGeI_3$ and b) $MASnI_3$. Structures are rendered with OVITO,[57] with the Ge/Sn bonds to neighboring iodine atoms shown. The blue arrows for the B-site indicate the off-centering displacements (relative to the neighboring iodine atoms), and the red arrows indicate the $\boldsymbol{r}_{\mathrm{NC}}$ vectors, pointing in the direction of the MA dipole.

The B-site off-centering is accompanied by pronounced orientational ordering of the organic sublattice, particularly in the Ge-rich compositions. The MA^+ cation carries a formal charge of 1 e that is distributed asymmetrically between its two ends, with the ammonium

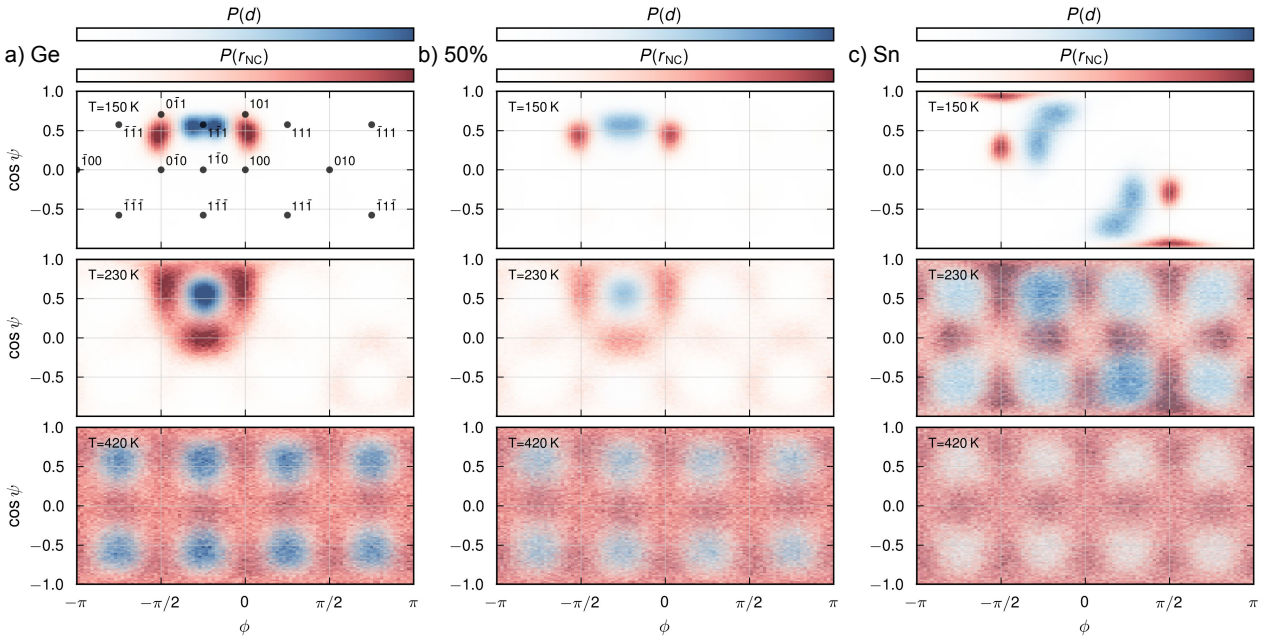

Figure 5: Distributions of the directions of the MA bond vectors ($\boldsymbol{r}_{\mathrm{NC}}$, red) and the B-site off-centering displacements ($\boldsymbol{d}$, blue) in a) Ge, b) the 50 % mixture, and c) Sn, shown as a function of the spherical angles ϕ and ψ at 150 K, 230 K, and 420 K. The distributions are averaged over several snapshots corresponding to roughly ± 10 K. Blue maxima mark the directions of the B-site displacements and red maxima the directions of the MA bond vectors, so that adjacent blue and red maxima indicate alignment of the two. Each map covers the full sphere of directions; the eight blue maxima at 420 K thus correspond to the eight $\langle 111 \rangle$ directions of the dynamically disordered off-centering. Selected crystallographic directions are indicated in a), and the same mapping applies to all panels. The polar angle is plotted as $\cos\psi$ rather than ψ, so that equal areas on the map correspond to equal solid angles and an isotropic distribution of orientations appears uniform. Note that the color scales differ between temperatures in order to most clearly show the underlying distributions; in addition, the Sn panels in c) use different color scales at 150 K and 230 K than those in a, b).

group (NH_3) holding the larger share. The molecule therefore carries a dipole moment directed from the methyl toward the ammonium group, i.e., along $\boldsymbol{r}_{\mathrm{NC}}$. The relationship and strong correlation between the molecular orientations and the B-site displacement directions can be visualized directly in the structural snapshots from the MD simulations (Figure 4). For Ge (Figure 4a), the MA cations clearly tend to point along the $\langle 110 \rangle$ directions nearest to the $\langle 111 \rangle$ Ge displacement direction, demonstrating a strong correlation between these two dipoles. For Sn (Figure 4b), the situation is more complex, since the Sn atoms partly adopt AFE distortions with alternating displacement directions, and the MA orientations follow the same alternating pattern.

The alignment of the B-site off-centering and the MA bond-vector orientation can be further quantified by considering the full distributions of the directions of $\boldsymbol{d}$ and $\boldsymbol{r}_{\mathrm{NC}}$ (Figure 5). The directions are represented by the spherical angles ϕ and ψ, where ϕ denotes the azimuthal angle in the xy plane and ψ the polar angle measured from the z axis. At 150 K, all Ge atoms are off-centered along the same direction, corresponding to one of the eight $\langle 111 \rangle$ directions, and the MA cations adopt only two preferred orientations, both of $\langle 110 \rangle$ type and lying close to the off-centering direction. This strong alignment persists to elevated temperatures. At 230 K, in the tilt-free intermediate phase, the MA cations explore a wider range of orientations and a third $\langle 110 \rangle$-type orientation becomes populated, while the alignment with the Ge off-centering direction is retained. This can be rationalized geometrically: for off-centering along, e.g., [111], the three directions [110], [101], and [011] all lie close to the off-centering axis, and the appearance of the third orientation is consistent with these directions becoming equivalent once the octahedral tilt is lost. Upon the transition into the cubic phase, the Ge displacements enter the DDO state, remaining locally off-centered while losing their long-range directional order, and consequently the MA cations lose their preferred orientations at the same transition. The distinct thermal evolution of the B-site and MA global ordering is shown in Figure S3. In $MAGeI_3$, the MA orientational order weakens progressively on heating, consistent with thermally activated reorientation, whereas the Ge

polar order remains robust until sharply dropping to zero at the cubic transition. The alignment reflects collective lattice ordering, with no notable additional nearest-neighbor angular correlation (Figure S4). The B-site and MA correlation is therefore not local in nature, but instead reflects the long-range order of the structure as a whole.

The 50 % mixture shows the same qualitative trend as the Ge system, but the distributions of both the MA orientations and the B-site displacements are more diffuse. This indicates that the preferred orientations are less strongly favored and that a larger degree of dynamic disorder is present in the mixed system. For Sn, the picture is qualitatively different: the AFE pattern of the B-site displacements gives rise to two distinct displacement orientations at 150 K. This is accompanied by a bimodal distribution of the MA bond vectors, whose maxima largely coincide with the two Sn displacement directions, showing that the MA orientations align with the long-range B-site displacement pattern. With increasing temperature, these narrow distributions broaden and become diffuse, and the system eventually becomes dynamically disordered with respect to both the molecular orientations and the off-centering.

Taken together, our results support a picture in which B-site off-centering reshapes the MA orientational landscape. In Ge-rich compositions, the strong polar $\langle 111 \rangle$ distortion favors a restricted set of MA orientations whose molecular dipoles align with the inorganic polar distortion, in contrast to the broader and dynamically disordered MA orientational landscape in tetragonal $MAPbI_3$.[35,37,41] Sn-rich compositions show a qualitatively different molecular ordering associated with the partially antipolar B-site displacement pattern. B-site mixing can therefore provide a tunable handle for selecting preferred molecular orientations and coupled polar or antipolar ordering patterns in hybrid halide perovskites.

Combining a MLIP with large-scale MD simulations, we have mapped the structural phase behavior of the mixed hybrid halide perovskite $MAGe_{1-x}Sn_xI_3$ across the full composition range. The phase diagram is governed by the competition between FE off-centering on the Ge-rich side and AFE off-centering tendencies combined with octahedral tilting on the

Sn-rich side, with the crossover between the two regimes located at roughly 65 % Sn. In the high-temperature phases, the off-centering enters a DDO state, in which the B-site cations remain locally displaced without long-range directional order. We further find correlated long-range ordering of the MA orientations and the B-site displacement patterns, although their thermal evolution differs markedly. On the Ge-rich side, the MA orientational order weakens progressively on heating while the long-range Ge displacement order remains robust until the cubic transition, consistent with a soft multi-minimum molecular landscape in which the ordered inorganic framework favors orientations aligned with the polar distortion. The qualitatively different molecular ordering in Sn-rich compositions shows that B-site mixing can tune the MA orientational landscape and the resulting polar or antipolar ordering patterns. Whether increasing molecular disorder contributes to the abrupt loss of Ge long-range order remains an open question.

Methods

DFT

DFT calculations were carried out using the all-electron electronic-structure code FHI-AIMS.[58] We employed the r^{2}SCAN50 hybrid functional,[59,60] which admixes 50 % exact exchange, together with the *intermediate* default basis set.[58] No additional dispersion correction was applied. This functional has been shown to be accurate for phase transitions in Ge perovskites.[27,55] The fraction of exact exchange sets the energy difference between the off-centered $R3m$ and cubic structures, and, most importantly, among PBE, r^{2}SCAN, r^{2}SCAN25, and r^{2}SCAN50 it is the 50 % admixture that yields phase-transition temperatures in agreement with experiment.[27,55]

Scalar relativistic effects were treated using the atomic zeroth-order regular approximation (atomic ZORA). The electronic self-consistency cycle was converged to an electron-density threshold of $10^{-6}\,\mathrm{e/a_0}^3$.

Brillouin-zone integrations were performed using automatically generated k-point meshes based on a k-point density parameter of 5.6, corresponding to an approximate reciprocal-space sampling of 0.18/Å.

qNEP construction and training

We constructed a qNEP[49,61,62] using the GPUMD package (version 4.8).[63,64] In this framework, each atomic partial charge is predicted by a neural network from the local descriptor vector, and electrostatic interactions are evaluated using qNEP mode 1, which includes real-space, reciprocal-space, and self-energy contributions. We additionally included the screened nuclear repulsion potential of Ziegler, Biersack, and Littmark[65] as a short-range baseline, as implemented in GPUMD.[66] The training set was built in an iterative way: starting from an initial set of structures, we repeatedly added snapshots drawn from MD simulations spanning a range of supercell sizes (up to 200 atoms) and temperatures, together with newly identified low-energy structures, and retrained the model at each iteration. The initial candidate set combined reported $MAGeI_3$ and $MASnI_3$ structures,[6,19] calculated Materials Project structures `mp-995236`, `mp-995238`, and `mp-1094059`,[67] and $MAPbI_3$-derived prototypes in which Pb was replaced by Ge or Sn. The final potential was trained on 668 structures. The training (test) root-mean-square errors are 4.33 meV/atom (7.67 meV/atom) for energies, 126 meV/Å (188 meV/Å) for forces, 19.9 meV/atom (18.5 meV/atom) for virials, and 0.0716 e (0.0596 e) for Born effective charges. The corresponding parity plots are shown in Figure S1.

Molecular dynamics

All structure handling and the interface to GPUMD were managed through ASE[68] and CALORINE.[69] Production MD simulations were performed with GPUMD[63,64] using a timestep of 0.5 fs and supercells containing 49 152 atoms. In all mixed supercells, Ge and Sn were assigned randomly to the B-site sublattice, and the resulting occupational configuration remained fixed throughout each MD trajectory.

All simulations were run in the NPT ensemble using stochastic cell rescaling,[70] as implemented in GPUMD. Phase transitions are observed through heating runs, which are ramped in temperature continuously from 0 K to 450 K over 20 ns, see Figure S2 for convergence testing.

We characterized the local and global structure across composition and temperature through three quantities, which serve as order parameters for identifying the structural phases of the system (see Figure 1a,b). Local octahedral tilt angles, θ_i^α, for B-site atom i in direction α were computed following the procedure of Ref.[71] The orientation of each MA cation was tracked through its C–N bond vector, $\boldsymbol{r}_{\mathrm{NC}} = \boldsymbol{r}_{\mathrm{N}} - \boldsymbol{r}_{\mathrm{C}}$. The B-site off-centering was quantified by the displacement

$$\boldsymbol{d} = \boldsymbol{r}_{\mathrm{B}} - \frac{1}{6}\sum_{i=1}^{6} \boldsymbol{r}_{\mathrm{I},i}, \tag{1}$$

where $\boldsymbol{r}_{\mathrm{B}}$ is the position of the Ge or Sn atom and the second term is the geometric center of the surrounding octahedron, defined by its six neighboring iodine atoms. A related distortion parameter that measures the B-site off-centering is the off-centering distortion $\mathcal{D}$ introduced in Ref. 24, defined as

$$\mathcal{D} = \sum_{\alpha=1}^{3} \frac{|a_\alpha - b_\alpha|}{a_\alpha + b_\alpha}, \tag{2}$$

where a_α and b_α are the short and long B–I bond lengths along the three trans I–B–I axes of the BI_6 octahedron. Unlike $\boldsymbol{d}$, $\mathcal{D}$ is dimensionless and directly accessible from diffraction, which enables a comparison with experimental values.

Octahedral tilting and $\langle 111 \rangle$ off-centering transform under different irreducible representations and cannot hybridize directly, although they compete energetically.[12,14] We therefore track them as separate order parameters. Here, the labels FE and AFE describe ferroic and antiferroic spatial patterns of B-site off-centering, respectively. The phases and transitions were identified using these order parameters from heating runs across the composition range,

together with the lattice parameters. Additionally, these order parameters, which are local in nature, were also used to get a better understanding of the local structure of the systems.

Acknowledgement

Funding from the Swedish Foundation for Strategic Research through the Future Research Leader programme (FFL21-0129), the Swedish Energy Agency (grant No. 45410-1), the Swedish Research Council (grant Nos. 2018-06482, 2019-03993, 2020-04935, 2025-03999, and 2025-04685), the European Research Council (ERC Starting Grant No. 101162195), the Knut and Alice Wallenberg Foundation (grant Nos. 2023.0032 and 2024.0042), and the Area of Advance Nano at Chalmers is gratefully acknowledged. The computations were enabled by resources provided by the National Academic Infrastructure for Supercomputing in Sweden (NAISS) at C3SE, PDC, and NSC, partially funded by the Swedish Research Council through grant agreement No. 2022-06725, as well as by the Berzelius resource provided by the Knut and Alice Wallenberg Foundation at NSC.

The authors used AI tools (Claude, Anthropic, and ChatGPT, OpenAI) during the preparation of this manuscript for assistance with writing and language improvements. All scientific content, interpretation, and final wording were reviewed and approved by the authors.

Supporting Information Available

Parity plots for the qNEP; convergence tests with respect to system size, heating rate and independent trajectories; global B-site and MA order parameters; the angle between the B-site off-centering and the MA orientation; potential energies along heating and cooling runs; and composition-resolved distributions of tilt angles and off-centering displacements for $x = 0.0$ to 1.0.

Data availability statement

The qNEP model and reference DFT data generated in this study are openly available via Zenodo at `https://doi.org/10.5281/zenodo.21863901`.

Notes

The authors declare no competing financial interest.

References

(1) National Renewable Energy Laboratory Best Research-Cell Efficiency Chart. 2026; `https://www.nrel.gov/pv/cell-efficiency.html`, accessed 2026-08-02.

(2) Ke, W.; Kanatzidis, M. G. Prospects for Low-Toxicity Lead-Free Perovskite Solar Cells. *Nat. Commun.* **2019**, *10*, 965.

(3) Hao, F.; Stoumpos, C. C.; Cao, D. H.; Chang, R. P. H.; Kanatzidis, M. G. Lead-Free Solid-State Organic-Inorganic Halide Perovskite Solar Cells. *Nat. Photonics* **2014**, *8*, 489–494.

(4) Noel, N. K.; Stranks, S. D.; Abate, A.; Wehrenfennig, C.; Guarnera, S.; Haghighirad, A.-A.; Sadhanala, A.; Eperon, G. E.; Pathak, S. K.; Johnston, M. B. et al. Lead-Free Organic-Inorganic Tin Halide Perovskites for Photovoltaic Applications. *Energy Environ. Sci.* **2014**, *7*, 3061–3068.

(5) Krishnamoorthy, T.; Ding, H.; Yan, C.; Leong, W. L.; Baikie, T.; Zhang, Z.; Sherburne, M.; Li, S.; Asta, M.; Mathews, N. et al. Lead-Free Germanium Iodide Perovskite Materials for Photovoltaic Applications. *J. Mater. Chem. A* **2015**, *3*, 23829–23832.

(6) Stoumpos, C. C.; Frazer, L.; Clark, D. J.; Kim, Y. S.; Rhim, S. H.; Freeman, A. J.; Ketterson, J. B.; Jang, J. I.; Kanatzidis, M. G. Hybrid Germanium Iodide Perovskite Semiconductors: Active Lone Pairs, Structural Distortions, Direct and Indirect Energy Gaps, and Strong Nonlinear Optical Properties. *J. Am. Chem. Soc.* **2015**, *137*, 6804–6819.

(7) Mitzi, D. B.; Feild, C. A.; Schlesinger, Z.; Laibowitz, R. B. Transport, Optical, and Magnetic Properties of the Conducting Halide Perovskite $CH_3NH_3SnI_3$. *J. Solid State Chem.* **1995**, *114*, 159–163.

(8) Ito, N.; Kamarudin, M. A.; Hirotani, D.; Zhang, Y.; Shen, Q.; Ogomi, Y.; Iikubo, S.; Minemoto, T.; Yoshino, K.; Hayase, S. Mixed Sn–Ge Perovskite for Enhanced Perovskite Solar Cell Performance in Air. *J. Phys. Chem. Lett.* **2018**, *9*, 1682–1688.

(9) Chen, M.; Ju, M.-G.; Garces, H. F.; Carl, A. D.; Ono, L. K.; Hawash, Z.; Zhang, Y.; Shen, T.; Qi, Y.; Grimm, R. L. et al. Highly Stable and Efficient All-Inorganic Lead-Free Perovskite Solar Cells with Native-Oxide Passivation. *Nat. Commun.* **2019**, *10*, 16.

(10) Kama, A.; Tirosh, S.; Itzhak, A.; Ejgenberg, M.; Cahen, D. New Pb-Free Stable Sn-Ge Solid Solution Halide Perovskites Fabricated by Spray Deposition. *ACS Appl. Energy Mater.* **2022**, *5*, 3638–3646.

(11) Zhao, Z.; Sun, M.; Ji, Y.; Mao, K.; Huang, Z.; Yuan, C.; Yang, Y.; Ding, H.; Yang, Y.; Li, Y. et al. Efficient Homojunction Tin Perovskite Solar Cells Enabled by Gradient Germanium Doping. *Nano Lett.* **2024**, *24*, 5513–5520.

(12) Radha, S. K.; Bhandari, C.; Lambrecht, W. R. L. Distortion Modes in Halide Perovskites: To Twist or to Stretch, a Matter of Tolerance and Lone Pairs. *Phys. Rev. Mater.* **2018**, *2*, 063605.

(13) Li, X.; Guan, Y.; Li, X.; Fu, Y. Stereochemically Active Lone Pairs and Nonlinear Optical Properties of Two-Dimensional Multilayered Tin and Germanium Iodide Perovskites. *J. Am. Chem. Soc.* **2022**, *144*, 18030–18042.

(14) Hylton-Farrington, C. M.; Remsing, R. C. Octahedral Tilting and B-Site Off-Centering in Halide Perovskites Are Not Coupled. *Nat. Commun.* **2026**, *17*, 4345.

(15) Dalpian, G. M.; Zhao, X.-G.; Kazmerski, L.; Zunger, A. Formation and Composition-Dependent Properties of Alloys of Cubic Halide Perovskites. *Chem. Mater.* **2019**, *31*, 2497–2506.

(16) Im, J.; Stoumpos, C. C.; Jin, H.; Freeman, A. J.; Kanatzidis, M. G. Antagonism between Spin-Orbit Coupling and Steric Effects Causes Anomalous Band Gap Evolution in the Perovskite Photovoltaic Materials $CH_3NH_3Sn_{1-x}Pb_xI_3$. *J. Phys. Chem. Lett.* **2015**, *6*, 3503–3509.

(17) Rimkus, G.; Balčiūnas, S.; Petrosova, H. R.; Kucheriv, O. I.; Lemežis, R.; Klimavičius, V.; Kalendra, V.; Banys, J.; Gural'skiy, I. A.; Šimėnas, M. B-Site Mixing Effects in Hybrid Perovskites: Phase Transitions and Dielectric Response of $MAPb_{1-x}Sn_xBr_3$. *Chem. Mater.* **2025**, *37*, 1314–1320.

(18) Ju, M.-G.; Dai, J.; Ma, L.; Zeng, X. C. Lead-Free Mixed Tin and Germanium Perovskites for Photovoltaic Application. *J. Am. Chem. Soc.* **2017**, *139*, 8038–8043.

(19) Stoumpos, C. C.; Malliakas, C. D.; Kanatzidis, M. G. Semiconducting Tin and Lead Iodide Perovskites with Organic Cations: Phase Transitions, High Mobilities, and Near-Infrared Photoluminescent Properties. *Inorg. Chem.* **2013**, *52*, 9019–9038.

(20) Takahashi, Y.; Obara, R.; Lin, Z.-Z.; Takahashi, Y.; Naito, T.; Inabe, T.; Ishibashi, S.; Terakura, K. Charge-Transport in Tin-Iodide Perovskite $CH_3NH_3SnI_3$: Origin of High Conductivity. *Dalton Trans.* **2011**, *40*, 5563–5568.

(21) Yang, R. X.; Skelton, J. M.; da Silva, E. L.; Frost, J. M.; Walsh, A. Spontaneous Octahedral Tilting in the Cubic Inorganic Cesium Halide Perovskites $CsSnX_3$ and $CsPbX_3$ (X = F, Cl, Br, I). *J. Phys. Chem. Lett.* **2017**, *8*, 4720–4726.

(22) Fabini, D. H.; Honasoge, K.; Cohen, A.; Bette, S.; McCall, K. M.; Stoumpos, C. C.; Klenner, S.; Zipkat, M.; Hoang, L. P.; Nuss, J. et al. Noncollinear Electric Dipoles in a Polar Chiral Phase of $CsSnBr_3$ Perovskite. *J. Am. Chem. Soc.* **2024**, *146*, 15701–15717.

(23) Fabini, D. H.; Laurita, G.; Bechtel, J. S.; Stoumpos, C. C.; Evans, H. A.; Kontos, A. G.; Raptis, Y. S.; Falaras, P.; der Ven, A. V.; Kanatzidis, M. G. et al. Dynamic Stereochemical Activity of the Sn^{2+} Lone Pair in Perovskite $CsSnBr_3$. *J. Am. Chem. Soc.* **2016**, *138*, 11820–11832.

(24) Lü, X.; Stoumpos, C.; Hu, Q.; Ma, X.; Zhang, D.; Guo, S.; Hoffman, J.; Bu, K.; Guo, X.; Wang, Y. et al. Regulating Off-Centering Distortion Maximizes Photoluminescence in Halide Perovskites. *Natl. Sci. Rev.* **2021**, *8*, nwaa288.

(25) Parrott, E. S.; Milot, R.; Stergiopoulos, T.; Snaith, H.; Johnston, M.; Herz, L. Effect of Structural Phase Transition on Charge-Carrier Lifetimes and Defects in $CH_3NH_3SnI_3$ Perovskite. *J. Phys. Chem. Lett.* **2016**, *7*, 1321–1326.

(26) Zhang, Y.; Parsonnet, E.; Fernandez, A.; Griffin, S. M.; Huyan, H.; Lin, C.-K.; Lei, T.; Jin, J.; Barnard, E. S.; Raja, A. et al. Ferroelectricity in a Semiconducting All-Inorganic Halide Perovskite. *Sci. Adv.* **2022**, *8*, eabj5881.

(27) Kashikar, R.; Townsend, J.; Lisenkov, S.; Ponomareva, I. DFT-based insight into finite-temperature properties of ferroelectric perovskites with lone-pair: the case of $CsGeX_3$ (X = Cl, Br, I). *J. Phys.: Condens. Matter* **2026**, *38*, 015403.

(28) Zhao, Y.-Q.; Liu, B.; Yu, Z.-L.; Ma, J.; Wan, Q.; He, P.-B.; Cai, M.-Q. Strong Ferroelectric Polarization of $CH_3NH_3GeI_3$ with High-Absorption and Mobility Transport Anisotropy: Theoretical Study. *J. Mater. Chem. C* **2017**, *5*, 5356–5364.

(29) Hossain, K.; Khanom, S.; Israt, F.; Hossain, M.; Hossain, M. A.; Ahmed, F. First-Principles Study on Structural, Mechanical and Optoelectronic Properties of Lead-Free Mixed Ge–Sn Hybrid Organic-Inorganic Perovskites. *Solid State Commun.* **2020**, *320*, 114024.

(30) Nagane, S.; Ghosh, D.; Hoye, R. L. Z.; Zhao, B.; Ahmad, S.; Walker, A. B.; Islam, M. S.; Ogale, S.; Sadhanala, A. Lead-Free Perovskite Semiconductors Based on Germanium–Tin Solid Solutions: Structural and Optoelectronic Properties. *J. Phys. Chem. C* **2018**, *122*, 5940–5947.

(31) Li, J.; Rinke, P. Atomic Structure of Metal-Halide Perovskites from First Principles: The Chicken-and-Egg Paradox of the Organic-Inorganic Interaction. *Phys. Rev. B* **2016**, *94*, 045201.

(32) Ding, K.; Ye, H.; Su, C.; Xiong, Y.-A.; Du, G.; You, Y.-M.; Zhang, Z.-X.; Dong, S.; Zhang, Y.; Fu, D.-W. Superior Ferroelectricity and Nonlinear Optical Response in a Hybrid Germanium Iodide Hexagonal Perovskite. *Nat. Commun.* **2023**, *14*, 2863.

(33) Stroppa, A.; Quarti, C.; De Angelis, F.; Picozzi, S. Ferroelectric Polarization of $CH_3NH_3PbI_3$: A Detailed Study Based on Density Functional Theory and Symmetry Mode Analysis. *J. Phys. Chem. Lett.* **2015**, *6*, 2223–2231.

(34) Leguy, A. M. A.; Frost, J. M.; McMahon, A. P.; Sakai, V. G.; Kockelmann, W.; Law, C.; Li, X.; Foglia, F.; Walsh, A.; O'Regan, B. C. et al. The Dynamics of Methylammonium Ions in Hybrid Organic–Inorganic Perovskite Solar Cells. *Nat. Commun.* **2015**, *6*, 7124.

(35) Mattoni, A.; Filippetti, A.; Saba, M. I.; Delugas, P. Methylammonium Rotational Dynamics in Lead Halide Perovskite by Classical Molecular Dynamics: The Role of Temperature. *J. Phys. Chem. C* **2015**, *119*, 17421–17428.

(36) Chen, T.; Foley, B.; Ipek, B.; Tyagi, M.; Copley, J.; Brown, C.; Choi, J.; Lee, S.

Rotational dynamics of organic cations in the $CH_3NH_3PbI_3$ perovskite. *Phys. Chem. Chem. Phys.* **2015**, *17*, 31278–31286.

(37) Lahnsteiner, J.; Kresse, G.; Kumar, A.; Sarma, D. D.; Franchini, C.; Bokdam, M. Room-Temperature Dynamic Correlation between Methylammonium Molecules in Lead-Iodine-Based Perovskites: An Ab Initio Molecular Dynamics Perspective. *Phys. Rev. B* **2016**, *94*, 214114.

(38) Shimamura, K.; Hakamata, T.; Shimojo, F.; Kalia, R. K.; Nakano, A.; Vashishta, P. Rotation Mechanism of Methylammonium Molecules in Organometal Halide Perovskite in Cubic Phase: An Ab Initio Molecular Dynamics Study. *J. Chem. Phys.* **2016**, *145*, 224503.

(39) Li, J.; Bouchard, M.; Reiss, P.; Aldakov, D.; Pouget, S.; Demadrille, R.; Aumaitre, C.; Frick, B.; Djurado, D.; Rossi, M. et al. Activation Energy of Organic Cation Rotation in $CH_3NH_3PbI_3$ and $CD_3NH_3PbI_3$: Quasi-Elastic Neutron Scattering Measurements and First-Principles Analysis Including Nuclear Quantum Effects. *J. Phys. Chem. Lett.* **2018**, *9*, 3969–3977.

(40) Shuck, G.; Lehmann, F.; Ollivier, J.; Mutka, H.; Schorr, S. Influence of Chloride Substitution on the Rotational Dynamics of Methylammonium in $MAPbI_{3-x}Cl_x$ Perovskites. *J. Phys. Chem. C* **2019**, *123*.

(41) Fransson, E.; Rahm, J. M.; Wiktor, J.; Erhart, P. Revealing the Free Energy Landscape of Halide Perovskites: Metastability and Transition Characters in $CsPbBr_3$ and $MAPbI_3$. *Chem. Mater.* **2023**, *35*, 8229–8238.

(42) Lavén, R.; Koza, M. M.; Malavasi, L.; Perrichon, A.; Appel, M.; Karlsson, M. Rotational Dynamics of Organic Cations in Formamidinium Lead Iodide Perovskites. *J. Phys. Chem. Lett.* **2023**, *14*, 2784–2791.

(43) Swainson, I.; Chi, L.; Her, J.; Cranswick, L.; Stephens, P.; Winkler, B.; others Orientational Ordering, Tilting and Lone-Pair Activity in the Perovskite Methylammonium Tin Bromide, $CH_3NH_3SnBr_3$. *Acta Crystallogr., Sect. B* **2010**, *66*, 422–429.

(44) Ha, M.; Karmakar, A.; Bernard, G. M.; Basilio, E.; Krishnamurthy, A.; Askar, A. M.; Shankar, K.; Kroeker, S.; Michaelis, V. K. Phase Evolution in Methylammonium Tin Halide Perovskites with Variable Temperature Solid-State ^{119}Sn NMR Spectroscopy. *J. Phys. Chem. C* **2020**, *124*, 15015–15027.

(45) Kubicki, D. J.; Prochowicz, D.; Salager, E.; Rakhmatullin, A.; Grey, C. P.; Emsley, L.; Stranks, S. D. Local Structure and Dynamics in Methylammonium, Formamidinium, and Cesium Tin(II) Mixed-Halide Perovskites from ^{119}Sn Solid-State NMR. *J. Am. Chem. Soc.* **2020**, *142*, 7813–7826.

(46) Tang, L. C.; Huang, J. Y.; Chang, C. S.; Lee, M. H.; Liu, L. Q. New Infrared Nonlinear Optical Crystal $CsGeBr_3$: Synthesis, Structure and Powder Second-Harmonic Generation Properties. *J. Phys.: Condens. Matter* **2005**, *17*, 7275–7286.

(47) Lin, Z.-G.; Tang, L.-C.; Chou, C.-P. Characterization and Properties of Novel Infrared Nonlinear Optical Crystal $CsGe(Br_xCl_{1-x})_3$. *Inorg. Chem.* **2008**, *47*, 2362–2367.

(48) Qu, J.; Wang, Y.; Li, Z.; Li, M.; Pei, T.; Li, N.; Jiang, D.; Yang, B.; Li, B.; Ye, M. et al. Origin of Pressure-Induced Nonlinear Optical Property Enhancement in $CsGeCl_3$ Perovskite: $[GeCl_6]$ Octahedron Distortion and Band Gap Closing. *J. Am. Chem. Soc.* **2025**, *147*, 6717–6726.

(49) Fan, Z.; Zeng, Z.; Zhang, C.; Wang, Y.; Song, K.; Dong, H.; Chen, Y.; Ala-Nissila, T. Neuroevolution machine learning potentials: Combining high accuracy and low cost in atomistic simulations and application to heat transport. *Phys. Rev. B* **2021**, *104*, 104309.

(50) Fransson, E.; Wiktor, J.; Erhart, P. Phase transitions in inorganic halide perovskites from machine-learned potentials. *J. Phys. Chem. C* **2023**, *127*, 13773–13781.

(51) Hainer, T.; Fransson, E.; Dutta, S.; Wiktor, J.; Erhart, P. A Morphotropic Phase Boundary in $MA_{1-x}FA_xPbI_3$: Linking Structure, Dynamics, and Electronic Properties. *Nat. Commun.* **2025**, *16*, 8775.

(52) Laurita, G.; Fabini, D. H.; Stoumpos, C. C.; Kanatzidis, M. G.; Seshadri, R. Chemical Tuning of Dynamic Cation Off-Centering in the Cubic Phases of Hybrid Tin and Lead Halide Perovskites. *Chem. Sci.* **2017**, *8*, 5628–5635.

(53) Worhatch, R. J.; Kim, H.; Swainson, I. P.; Yonkeu, A. L.; Billinge, S. J. L. Study of Local Structure in Selected Organic–Inorganic Perovskites in the $Pm\bar{3}m$ Phase. *Chem. Mater.* **2008**, *20*, 1272–1277.

(54) Dutta, S.; Fransson, E.; Hainer, T.; Gallant, B. M.; Kubicki, D. J.; Erhart, P.; Wiktor, J. Revealing the Low-Temperature Phase of $FAPbI_3$ Using a Machine-Learned Potential. *J. Am. Chem. Soc.* **2025**, *147*, 37019–37029.

(55) Deswal, P.; Fransson, E.; Berger, E.; Ngoipala, A.; Dutta, S.; Erhart, P.; Wiktor, J. Exchange–Correlation Functional Dependence of Phase-Transition Temperatures in $CsGeBr_3$ Using Machine-Learned Potentials. 2026; Manuscript in preparation.

(56) Ozório, M. S.; Srikanth, M.; Besse, R.; Da Silva, J. L. F. The Role of the A-Cations in the Polymorphic Stability and Optoelectronic Properties of Lead-Free $ASnI_3$ Perovskites. *Phys. Chem. Chem. Phys.* **2021**, *23*, 2286–2297.

(57) Stukowski, A. Visualization and analysis of atomistic simulation data with OVITO–the Open Visualization Tool. *Modell. Simul. Mater. Sci. Eng.* **2010**, *18*, 015012.

(58) Blum, V.; Gehrke, R.; Hanke, F.; Havu, P.; Havu, V.; Ren, X.; Reuter, K.; Scheffler, M.

Ab initio molecular simulations with numeric atom-centered orbitals. *Comput. Phys. Commun.* **2009**, *180*, 2175–2196.

(59) Furness, J. W.; Kaplan, A. D.; Ning, J.; Perdew, J. P.; Sun, J. Accurate and Numerically Efficient r^{2}SCAN Meta-Generalized Gradient Approximation. *J. Phys. Chem. Lett.* **2020**, *11*, 8208–8215.

(60) Bursch, M.; Neugebauer, H.; Ehlert, S.; Grimme, S. Dispersion corrected r^{2}SCAN based global hybrid functionals: r^{2}SCANh, r^{2}SCAN0, and r^{2}SCAN50. *J. Chem. Phys.* **2022**, *156*, 134105.

(61) Fan, Z. Improving the accuracy of the neuroevolution machine learning potential for multi-component systems. *J. Phys.: Condens. Matter* **2022**, *34*, 125902.

(62) Fan, Z.; Tang, B.; Berger, E.; Berger, E.; Fransson, E.; Xu, K.; Yan, Z.; Liu, Z.; Song, Z.; Dong, H. et al. qNEP: A Highly Efficient Neuroevolution Potential with Dynamic Charges for Large-Scale Atomistic Simulations. *J. Chem. Theory Comput.* **2026**, *22*, 4787–4801.

(63) Fan, Z.; Wang, Y.; Ying, P.; Song, K.; Wang, J.; Wang, Y.; Zeng, Z.; Xu, K.; Lindgren, E.; Rahm, J. M. et al. GPUMD: A package for constructing accurate machine-learned potentials and performing highly efficient atomistic simulations. *J. Chem. Phys.* **2022**, *157*, 114801.

(64) Xu, K.; Bu, H.; Pan, S.; Lindgren, E.; Wu, Y.; Wang, Y.; Liu, J.; Song, K.; Xu, B.; Li, Y. et al. GPUMD 4.0: A high-performance molecular dynamics package for versatile materials simulations with machine-learned potentials. *Mater. Genome Eng. Adv.* **2025**, *3*, e70028.

(65) Ziegler, J. F.; Biersack, J. P.; Littmark, U. *The Stopping and Range of Ions in Matter*; Pergamon: New York, 1985; Vol. 1.

(66) Liu, D.; Zeng, H.; Peng, H.; Sa, R. Computational study of the fundamental properties of Zr-based chalcogenide perovskites for optoelectronics. *Phys. Chem. Chem. Phys.* **2023**, *25*, 13755–13765.

(67) Horton, M. K.; Huck, P.; Yang, R. X.; Munro, J. M.; Dwaraknath, S.; Ganose, A. M.; Kingsbury, R. S.; Wen, M.; Shen, J. X.; Mathis, T. S. et al. Accelerated Data-Driven Materials Science with the Materials Project. *Nat. Mater.* **2025**, *24*, 1522–1532.

(68) Larsen, A. H.; Mortensen, J. J.; Blomqvist, J.; Castelli, I. E.; Christensen, R.; Dułak, M.; Friis, J.; Groves, M. N.; Hammer, B.; Hargus, C. et al. The atomic simulation environment—a Python library for working with atoms. *J. Phys.: Condens. Matter* **2017**, *29*, 273002.

(69) Lindgren, E.; Rahm, M.; Fransson, E.; Eriksson, F.; Österbacka, N.; Fan, Z.; Erhart, P. calorine: A Python package for constructing and sampling neuroevolution potential models. *J. Open Source Software* **2024**, *9*, 6264.

(70) Bernetti, M.; Bussi, G. Pressure control using stochastic cell rescaling. *J. Chem. Phys.* **2020**, *153*, 114107.

(71) Wiktor, J.; Fransson, E.; Kubicki, D.; Erhart, P. Quantifying Dynamic Tilting in Halide Perovskites: Chemical Trends and Local Correlations. *Chem. Mater.* **2023**, *35*, 6737–6744.

Supporting Information

Interplay of B-site Off-centering and Molecular Orientations in the Mixed Hybrid Perovskite $MAGe_{1-x}Sn_xI_3$

Erik Fransson,[1] Apinya Ngoipala,[1] Oskar Öjstedt,[2] Maths Karlsson,[2]
Paul Erhart,[1] and Julia Wiktor[1,†]

[1] Department of Physics and Astronomy, Chalmers University of Technology, SE-412 96 Gothenburg, Sweden
[2] Department of Chemistry and Chemical Engineering, Chalmers University of Technology, SE-412 96 Gothenburg, Sweden
[†] julia.wiktor@chalmers.se

Contents

Supplementary Notes **S2**
SN1. Density functional theory calculations . . . S2
SN2. Neuroevolution potential construction . . . S2
SN3. Global B-site and MA order parameters . . . S2
SN4. B-site–MA orientational correlation . . . S3

Supplementary Figures **S4**
S1. Parity plots for the charge-aware neuroevolution potential . . . S4
S2. Convergence tests for the molecular-dynamics heating simulations . . . S5
S3. Global B-site and MA order parameters . . . S5
S4. Angle between the B-site off-centering and the MA orientation . . . S6
S5. Splitting of the B–iodine first coordination shell . . . S6
S6. Potential energy along the heating and cooling runs . . . S7
S7. Heating-induced evolution of octahedral tilting and B-site off-centering in MAGeI3 . . . S8
S8. Heating-induced evolution of octahedral tilting and B-site off-centering in MAGe0.9Sn0.1I3 . . . S8
S9. Heating-induced evolution of octahedral tilting and B-site off-centering in MAGe0.8Sn0.2I3 . . . S9
S10. Heating-induced evolution of octahedral tilting and B-site off-centering in MAGe0.7Sn0.3I3 . . . S9
S11. Heating-induced evolution of octahedral tilting and B-site off-centering in MAGe0.6Sn0.4I3 . . . S10
S12. Heating-induced evolution of octahedral tilting and B-site off-centering in MAGe0.5Sn0.5I3 . . . S10
S13. Heating-induced evolution of octahedral tilting and B-site off-centering in MAGe0.4Sn0.6I3 . . . S11
S14. Heating-induced evolution of octahedral tilting and B-site off-centering in MAGe0.3Sn0.7I3 . . . S11
S15. Heating-induced evolution of octahedral tilting and B-site off-centering in MAGe0.2Sn0.8I3 . . . S12
S16. Heating-induced evolution of octahedral tilting and B-site off-centering in MAGe0.1Sn0.9I3 . . . S12
S17. Heating-induced evolution of octahedral tilting and B-site off-centering in MASnI3 . . . S13

Supplementary References **S14**

Supplementary Notes

Supplementary Note 1: Density functional theory calculations

All density-functional theory (DFT) calculations were performed with the all-electron electronic-structure code FHI-AIMS (S1). We employed the r^{2}SCAN50 hybrid functional (S2, S3), which admixes 50 % exact exchange, together with the *intermediate* default basis set (S1). Scalar relativistic effects were treated using the atomic zeroth-order regular approximation (atomic ZORA). The electronic self-consistency cycle was converged to an electron-density threshold of 10^{-6} e/bohr^3. Brillouin-zone integrations were performed using automatically generated k-point meshes based on a k-point density parameter of 5.6, corresponding to an approximate reciprocal-space sampling of 0.18/Å.

Energies, forces, and virials were extracted from these calculations as reference data for the interatomic potential. Born effective charges were additionally computed for a few tens of selected structures containing fewer than 100 atoms and used as qNEP training targets.

Supplementary Note 2: Neuroevolution potential construction

We constructed a charge-aware neuroevolution potential (qNEP) using the GPUMD package (version 4.8) (S4–S6). In this framework, the short-range contribution to the energy is obtained from a neural network acting on local descriptor vectors, while a second network predicts an atomic partial charge from the same descriptors. The resulting electrostatic interactions are evaluated using qNEP mode 1, which includes real-space, reciprocal-space, and self-energy contributions (S6). We additionally included the screened nuclear repulsion potential ZBL from Ziegler, Biersack, and Littmark (S7) as a short-range baseline, as implemented in GPUMD (S8).

The training set was built iteratively in an active-learning loop. Starting from an initial set of structures, we repeatedly added snapshots drawn from molecular dynamics (MD) simulations spanning a range of supercell sizes (up to about 200 atoms) and temperatures, together with newly identified low-energy structures, and retrained the model at each iteration. The final model was trained on 668 structures.

The training and test parity plots are shown in Figure S1. The training (test) root-mean-square errors are 4.33 meV/atom (7.67 meV/atom) for energies, 126 meV/Å (188 meV/Å) for forces, 19.9 meV/atom (18.5 meV/atom) for virials, and 0.0716 e (0.0596 e) for Born effective charges.

The ASE (S9) and CALORINE (S10) packages were used to prepare the training structures, to set up the MD simulations, and to post-process the results.

Supplementary Note 3: Global B-site and MA order parameters

We characterize the collective ordering of the B-site and MA sublattices using three global order parameters evaluated separately for each MD frame. The net B-site off-centering, the global directional order of the B-site off-centering, and the global directional order of the MA orientations are defined as

$$P_{\mathrm{B}} = \left| \frac{1}{N_{\mathrm{B}}} \sum_{i=1}^{N_{\mathrm{B}}} \mathbf{d}_i \right|, \tag{1}$$

$$P_{\mathrm{B}}^{\mathrm{dir}} = \left| \frac{1}{N_{\mathrm{B}}} \sum_{i=1}^{N_{\mathrm{B}}} \hat{\mathbf{d}}_i \right|, \qquad \hat{\mathbf{d}}_i = \frac{\mathbf{d}_i}{|\mathbf{d}_i|}, \tag{2}$$

$$P_{\mathrm{MA}}^{\mathrm{dir}} = \left| \frac{1}{N_{\mathrm{MA}}} \sum_{j=1}^{N_{\mathrm{MA}}} \hat{\mathbf{r}}_{\mathrm{NC},j} \right|, \qquad \hat{\mathbf{r}}_{\mathrm{NC},j} = \frac{\mathbf{r}_{\mathrm{NC},j}}{|\mathbf{r}_{\mathrm{NC},j}|}. \tag{3}$$

Here, $\mathbf{d}_i$ is the displacement of B site i from the geometric center of its six-iodine octahedron, and $\mathbf{r}_{\mathrm{NC},j}$ is the N–C vector of MA molecule j. The quantity P_{B} has units of length and measures the net B-site off-centering. The directional order parameters $P_{\mathrm{B}}^{\mathrm{dir}}$ and $P_{\mathrm{MA}}^{\mathrm{dir}}$ are dimensionless and range from zero to one. They measure directional coherence independently of the local displacement or bond-vector magnitudes. All three quantities are calculated as instantaneous measures for each frame separately over the trajectory. For randomly oriented unit vectors both the directional order parameters $P_{\mathrm{B}}^{\mathrm{dir}}$ and $P_{\mathrm{MA}}^{\mathrm{dir}}$ would be zero.

The resulting temperature dependence is shown in Figure S3. For $MAGeI_3$ and the 50 % mixture, $P_{\mathrm{MA}}^{\mathrm{dir}}$ decreases progressively on heating, whereas the B-site order remains comparatively robust before dropping

to its disordered baseline at the cubic transition. For $MASnI_3$, P_{MA}^{dir} remains close to zero, while the B-site directional order is lost at the first structural transition. The similar evolution of P_B and P_B^{dir} shows that the loss of net B-site off-centering primarily reflects the loss of directional coherence rather than the disappearance of the local distortion.

Supplementary Note 4: B-site–MA orientational correlation

To quantify the orientational correlation between B-site off-centering and MA orientation, we define the angle

$$\alpha_{ij} = \arccos\left(\frac{\boldsymbol{d}_i \cdot \boldsymbol{r}_{NC,j}}{|\boldsymbol{d}_i|\,|\boldsymbol{r}_{NC,j}|}\right), \tag{4}$$

where $\boldsymbol{d}_i$ is the off-centering of B site i and $\boldsymbol{r}_{NC,j}$ is the N–C vector of molecule j. Each B site is surrounded by eight MA molecules. We compare two distributions of α_{ij}: a *local* distribution evaluated over these eight neighboring MA molecules and a *global* distribution evaluated between each B site and all MA molecules within the same frame. The global distribution retains the separate orientational distributions of both sublattices, including any long-range order, but is not restricted to neighboring pairs, so that comparison with the local distribution isolates the local part of the coupling. For uncorrelated vectors $\cos\alpha$ is uniformly distributed, giving $P(\alpha) = \frac{1}{2}\sin\alpha$ and $\langle\alpha\rangle = 90°$.

In the low-temperature phases of $MAGeI_3$ and $MAGe_{0.5}Sn_{0.5}I_3$, $P(\alpha)$ peaks near 45° and shifts toward 90° upon heating (Figure S4a,b). The mean angle reaches 90° at approximately 380 K and 280 K, respectively, i.e., at the temperatures at which the long-range polar order is lost (Figure S4d,e). For $MASnI_3$, $\langle\alpha\rangle$ equals 90° throughout, but below 200 K the distribution is bimodal, with lobes near 45° and 135° that cancel in the mean (Figure S4c,f). This bimodality is consistent with the alternating off-centering directions of the antiferroelectric components of the $MASnI_3$ ground state.

The local and global curves coincide over the entire temperature range. The low-temperature correlation is therefore a consequence of the long-range order: $\boldsymbol{d}$ and $\boldsymbol{r}_{NC}$ are each ordered with respect to the lattice, and thus no excess local correlation is observed. In the cubic phase, the angular distributions approach the isotropic reference for all systems, consistent with the loss of long-range B-site and MA orientational order, with no notable local angular correlation remaining.

Supplementary Figures

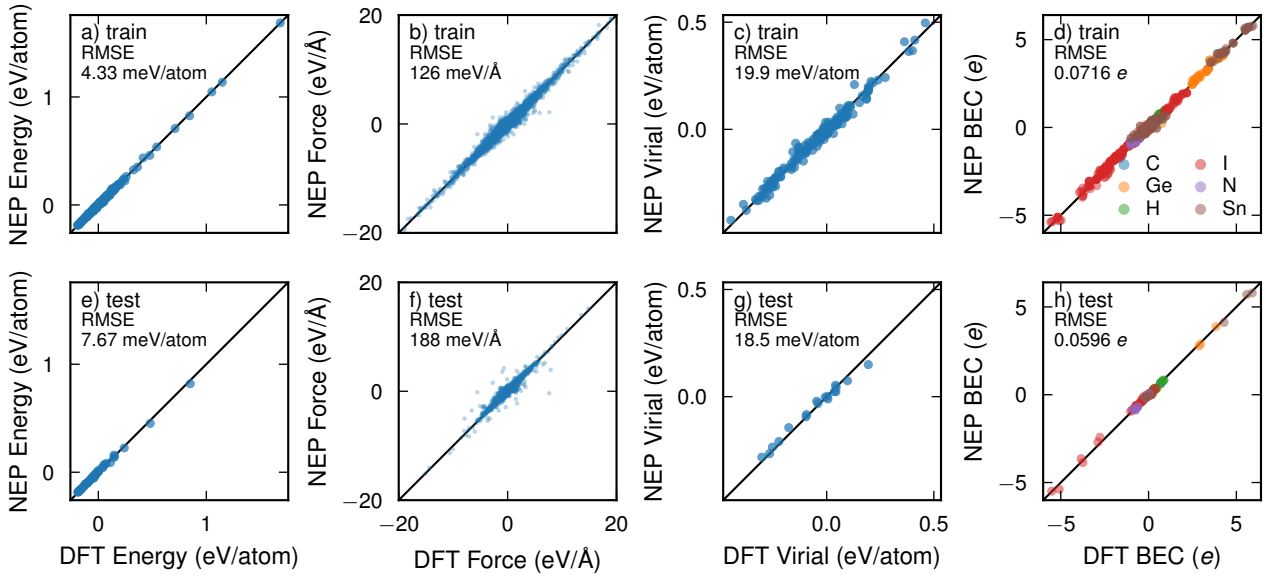

Figure S1: Parity plots for the $MAGe_{1-x}Sn_xI_3$ qNEP against the r^{2}SCAN50 reference data for the training set (a–d) and test set (e–h). The columns show energy, force, virial, and Born effective charge, with the root-mean-square error quoted in each panel. The Born-effective-charge points are colored by species.

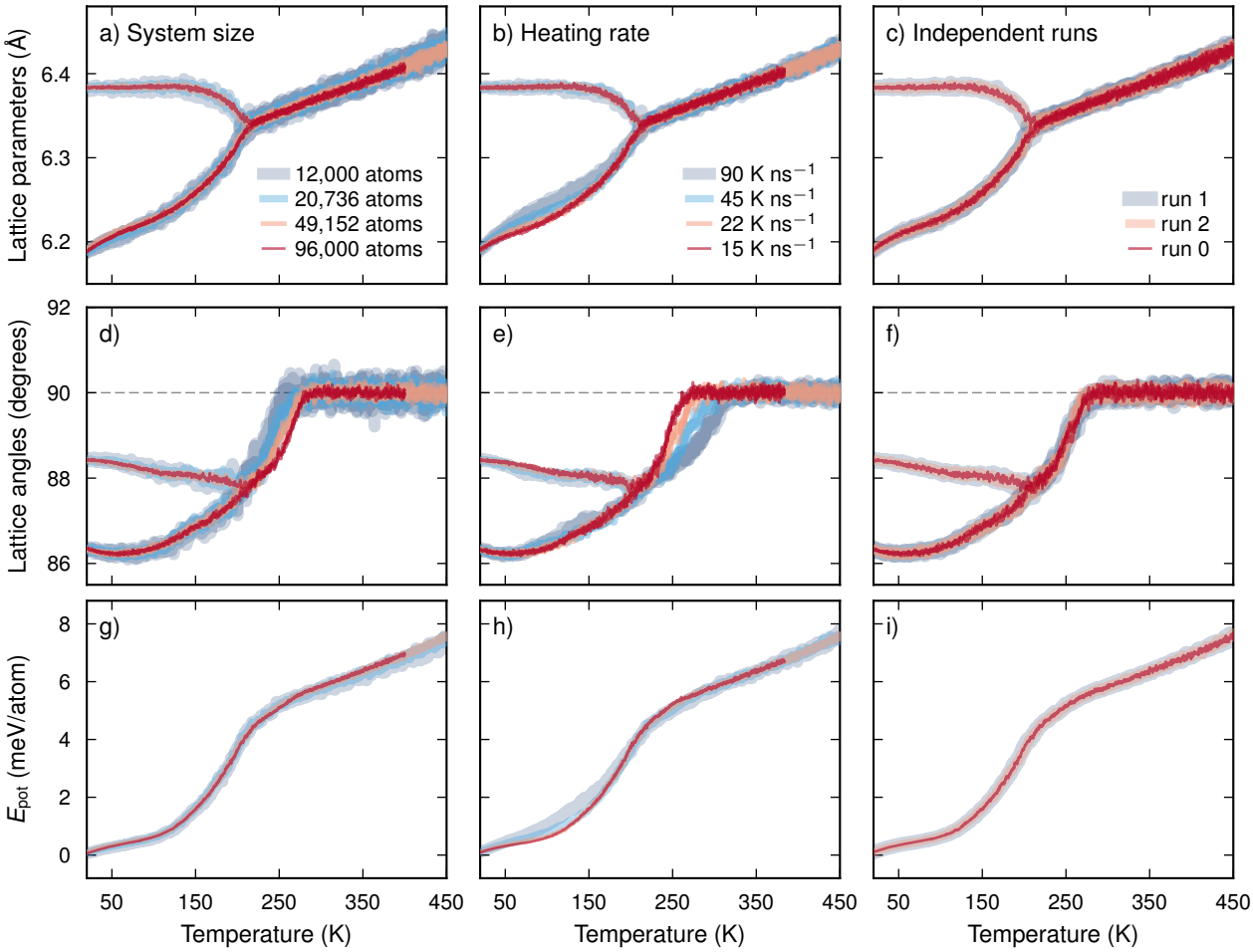

Figure S2: Convergence of the heating run for a 50 % mixture showing lattice parameters (a–c), lattice angles (d–f), and potential energy per atom (g–i) as functions of temperature. The columns compare system sizes of 12 000, 20 736, 49 152, and 96 000 atoms (a,d,g), heating rates of 15 K/ns, 22 K/ns, 45 K/ns, and 90 K/ns (b,e,h), and three independent heating trajectories (c,f,i) with 49 152 atoms and rate of 22 K/ns.

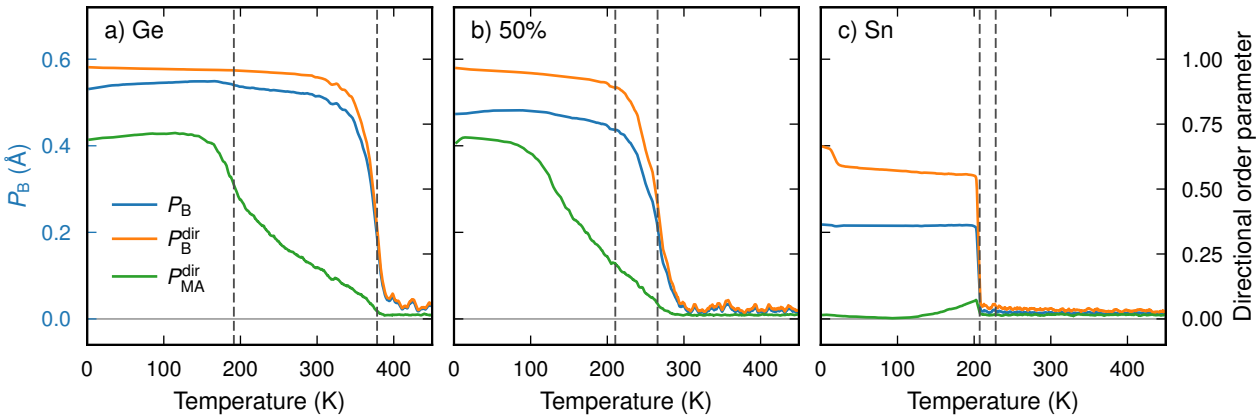

Figure S3: Global order parameters along the heating ramps of (a) $MAGeI_3$, (b) $MAGe_{0.5}Sn_{0.5}I_3$, and (c) $MASnI_3$. Each panel shows the net B-site off-centering P_B (blue, left axis) and the dimensionless directional order parameters P_B^{dir} (orange, right axis) and P_{MA}^{dir} (green, right axis). The vertical dashed lines mark the transition temperatures shown in the phase diagram. In (a) and (b), the first transition corresponds to the loss of octahedral tilting and the second to the loss of long-range B-site directional order and the transition to the cubic phase. In (c), the first transition corresponds to a change in the tilt pattern and the simultaneous loss of B-site directional order, while the second corresponds to the loss of the remaining tilt and the transition to the cubic phase.

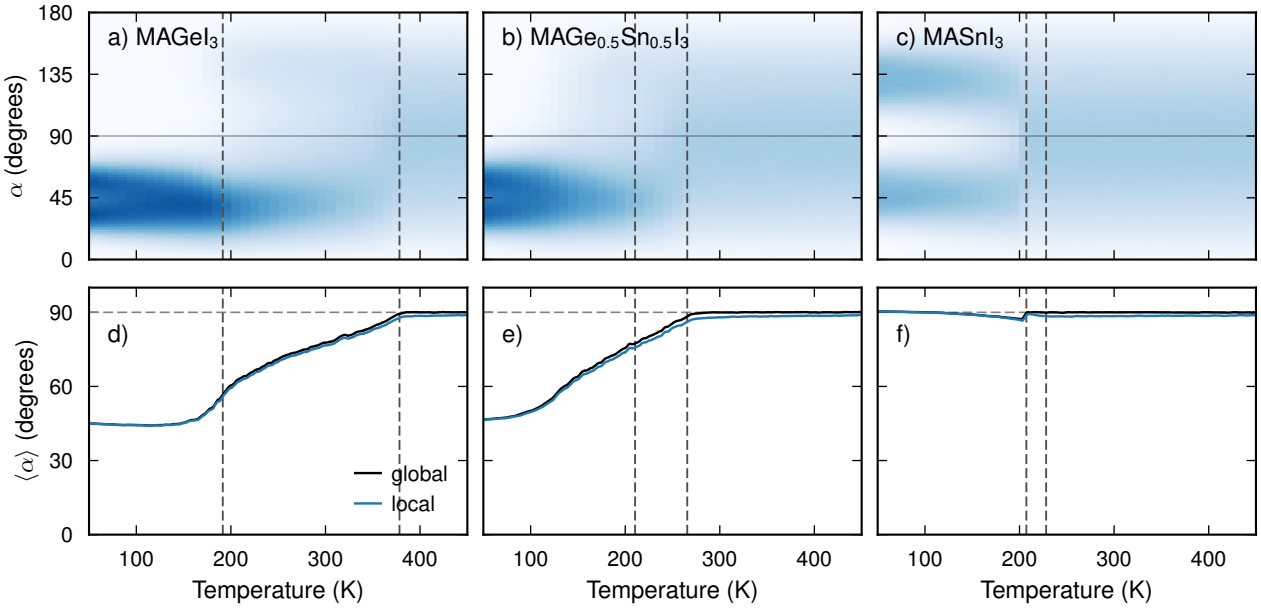

Figure S4: Angle α between the B-site off-centering $\boldsymbol{d}$ and the MA N–C vector $\boldsymbol{r}_{\mathrm{NC}}$ along the heating ramp. a)–c) Distribution $P(\alpha)$ over neighboring B-site/MA pairs. d)–f) Mean angle for neighboring pairs (local) and for all pairs (global). The dashed line marks the uncorrelated value $\langle\alpha\rangle = 90°$. The columns correspond to $MAGeI_3$, $MAGe_{0.5}Sn_{0.5}I_3$, and $MASnI_3$. The local and global curves are in close agreement, demonstrating that the B-site MA correlation follows the long-range order and not the local environment.

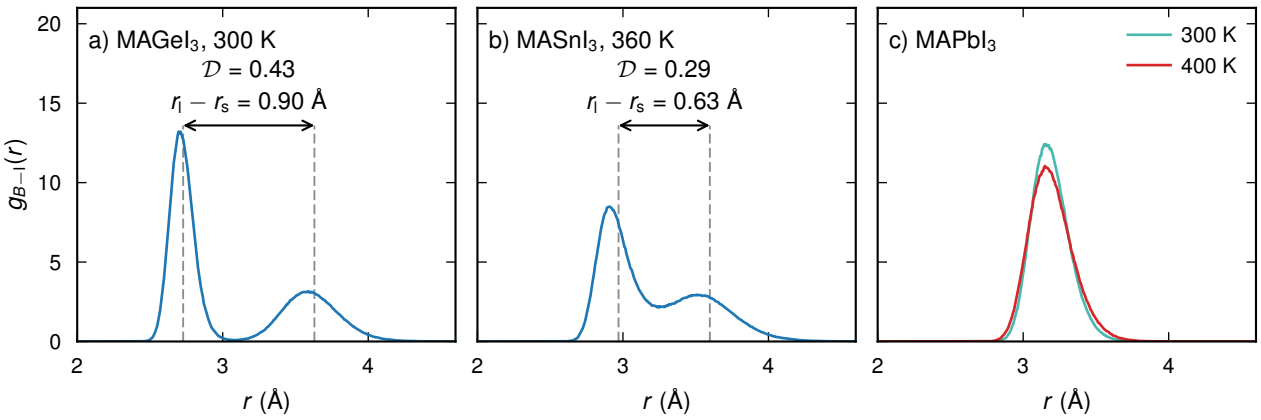

Figure S5: Partial radial distribution function $g_{B-\mathrm{I}}(r)$ between the B-site cation and iodine for a) $MAGeI_3$ at 300 K, b) $MASnI_3$ at 360 K, and c) $MAPbI_3$ at 300 K and 400 K. Each curve is calculated with OVITO by averaging over all snapshots from the corresponding heating run lying within 10 K of the stated temperature. $MAPbI_3$ is included as a reference for a B-site cation without any off-centering. The dashed lines in a) and b) mark the short and long B–I bond lengths r_{s} and r_{l}, each obtained as the mean of r over the corresponding part of the first coordination shell weighted by $g_{B-\mathrm{I}}(r)\,r^2$, with the two regions separated by the minimum between the peaks. The weighted means therefore need not coincide with the peak maxima, particularly for the asymmetric long-bond peak. $\mathcal{D}$ is the off-centering distortion parameter evaluated from r_{s} and r_{l}. For $MAPbI_3$, no splitting of the first coordination shell is resolved, corresponding to $\mathcal{D} = 0.0$.

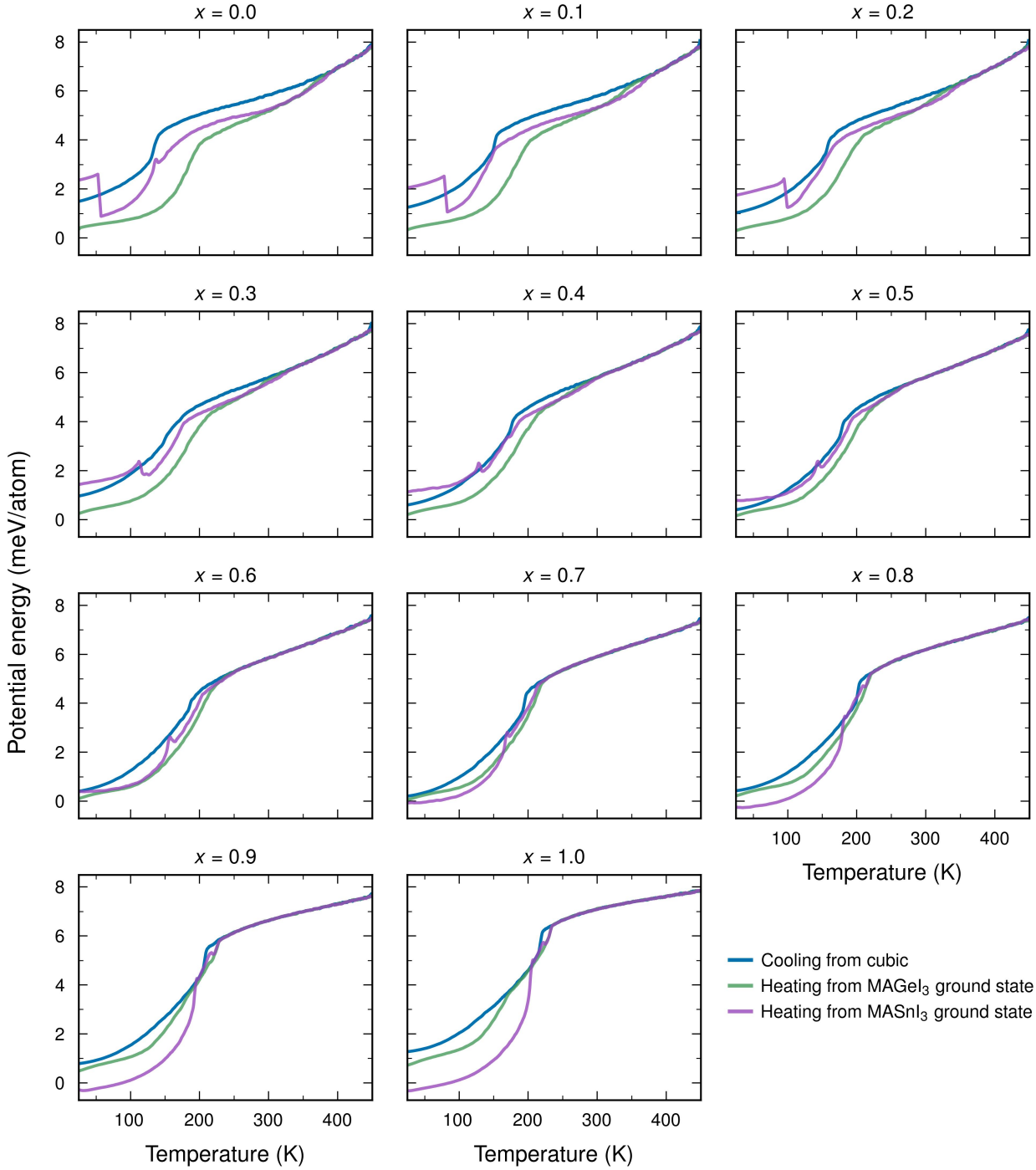

Figure S6: Potential energy as a function of temperature for mixed $MAGe_{1-x}Sn_xI_3$ (x = 0.0–1.0) during cooling from the cubic phase (blue) and heating from the $MAGeI_3$ (green) and $MASnI_3$ (purple) ground states. For each composition, the energy is referenced to the lowest potential energy among the three trajectories after subtracting the classical thermal contribution, $\frac{3}{2}k_BT$ per atom.

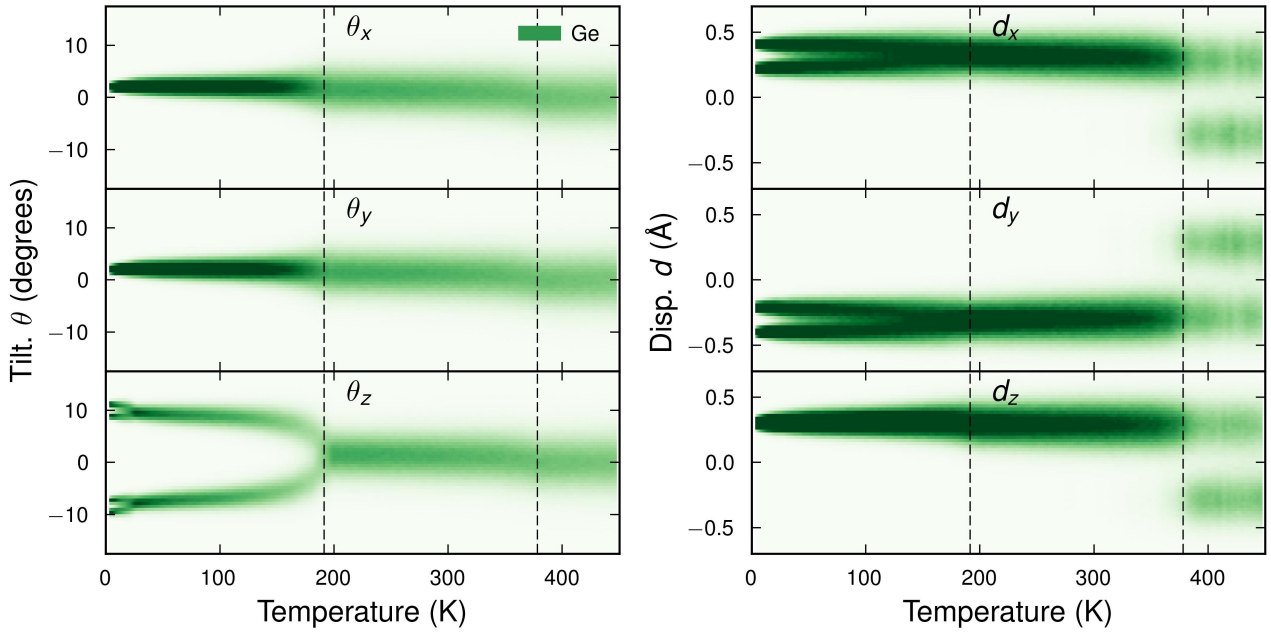

Figure S7: Temperature-dependent distributions of the octahedral tilt angles (θ; left) and B-site off-centering displacements (d; right) along the x, y, and z directions for $MAGeI_3$, with the Ge distribution shown in green. The vertical dashed lines denote the phase-transition temperatures.

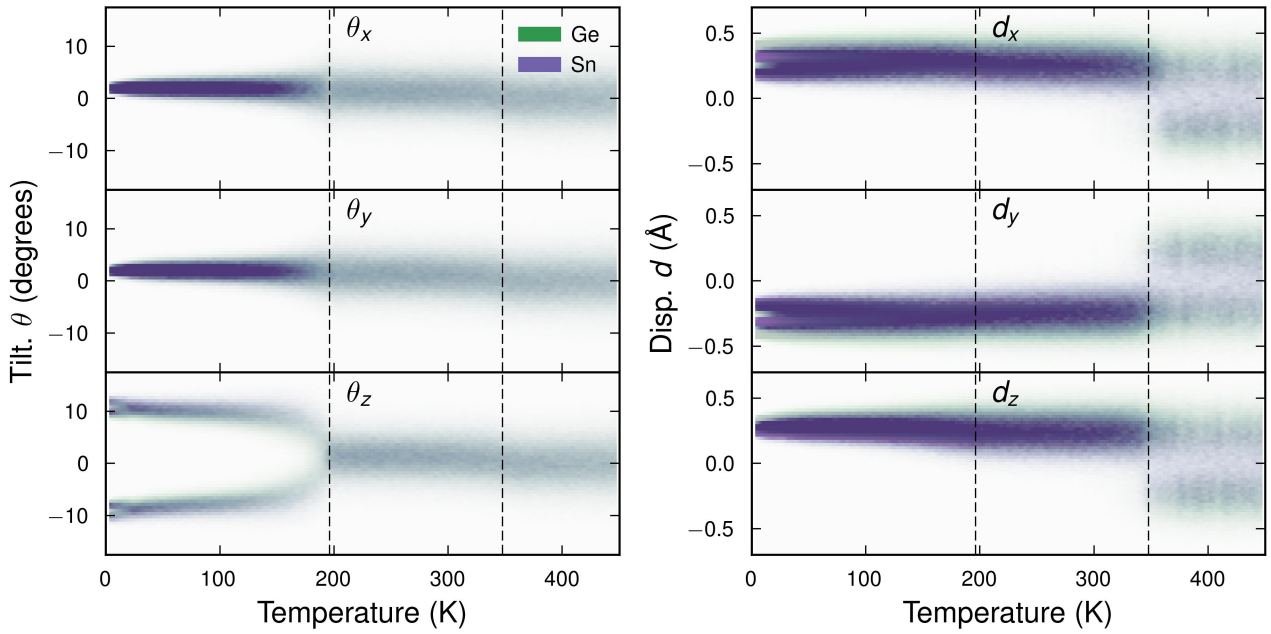

Figure S8: Temperature-dependent distributions of the octahedral tilt angles (θ; left) and B-site off-centering displacements (d; right) along the x, y, and z directions for $MAGe_{0.9}Sn_{0.1}I_3$, with the Ge and Sn distributions shown in green and purple, respectively. The vertical dashed lines denote the phase-transition temperatures.

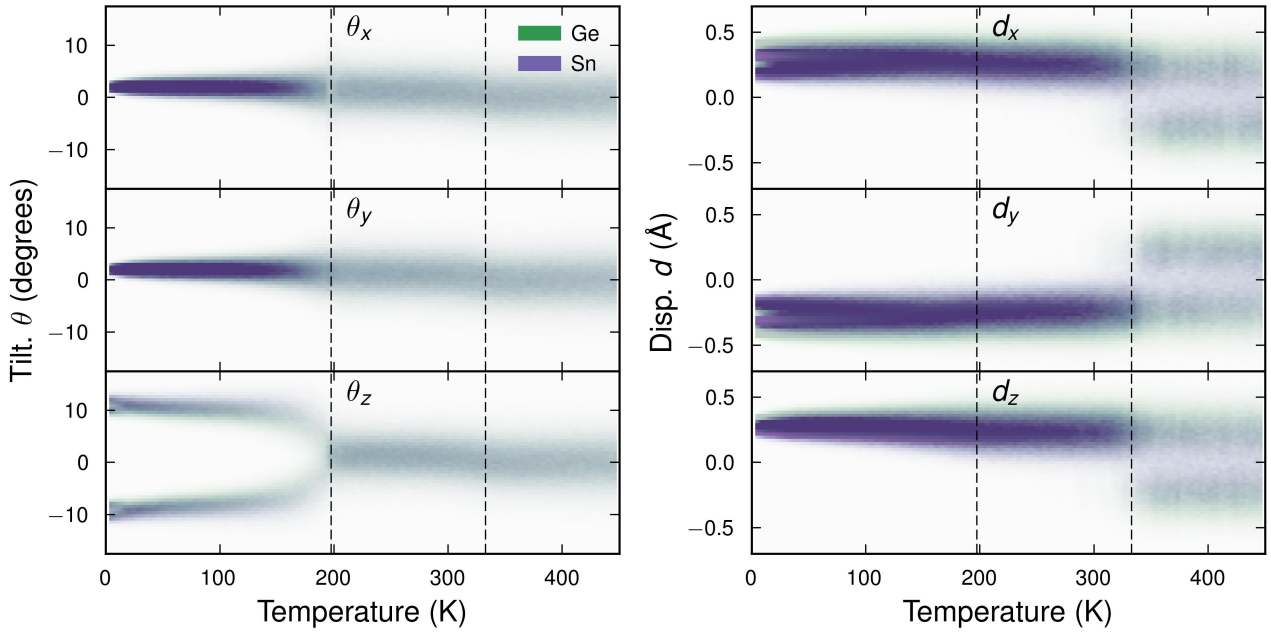

Figure S9: Temperature-dependent distributions of the octahedral tilt angles (θ; left) and B-site off-centering displacements (d; right) along the x, y, and z directions for $MAGe_{0.8}Sn_{0.2}I_3$, with the Ge and Sn distributions shown in green and purple, respectively. The vertical dashed lines denote the phase-transition temperatures.

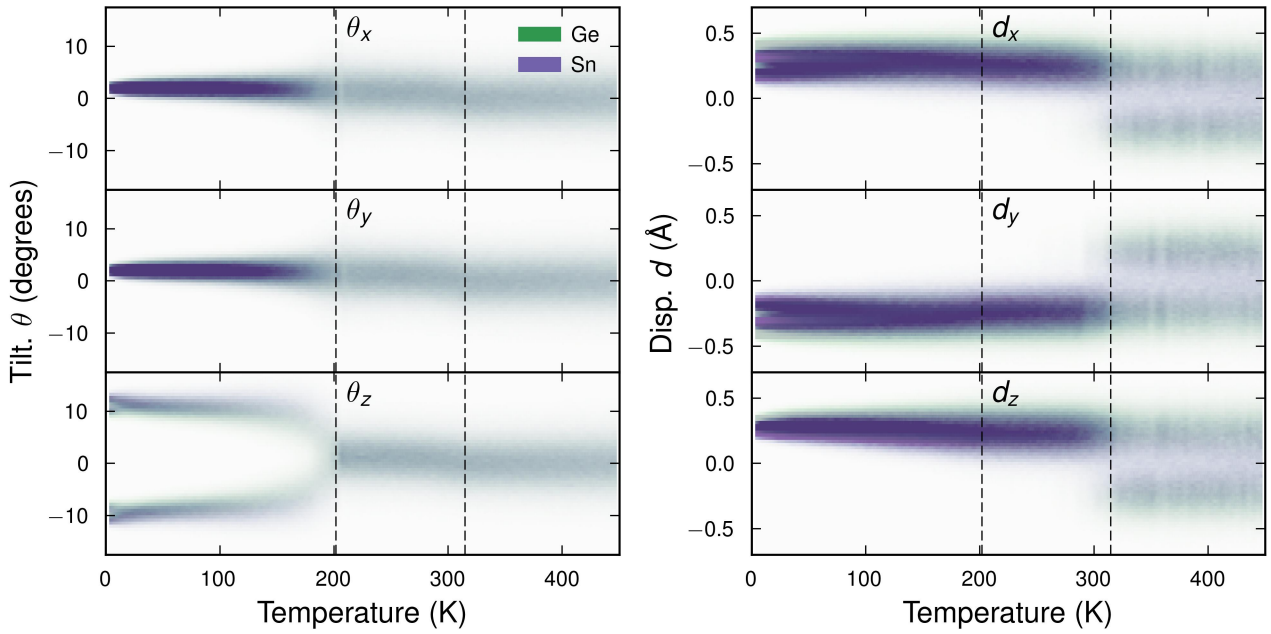

Figure S10: Temperature-dependent distributions of the octahedral tilt angles (θ; left) and B-site off-centering displacements (d; right) along the x, y, and z directions for $MAGe_{0.7}Sn_{0.3}I_3$, with the Ge and Sn distributions shown in green and purple, respectively. The vertical dashed lines denote the phase-transition temperatures.

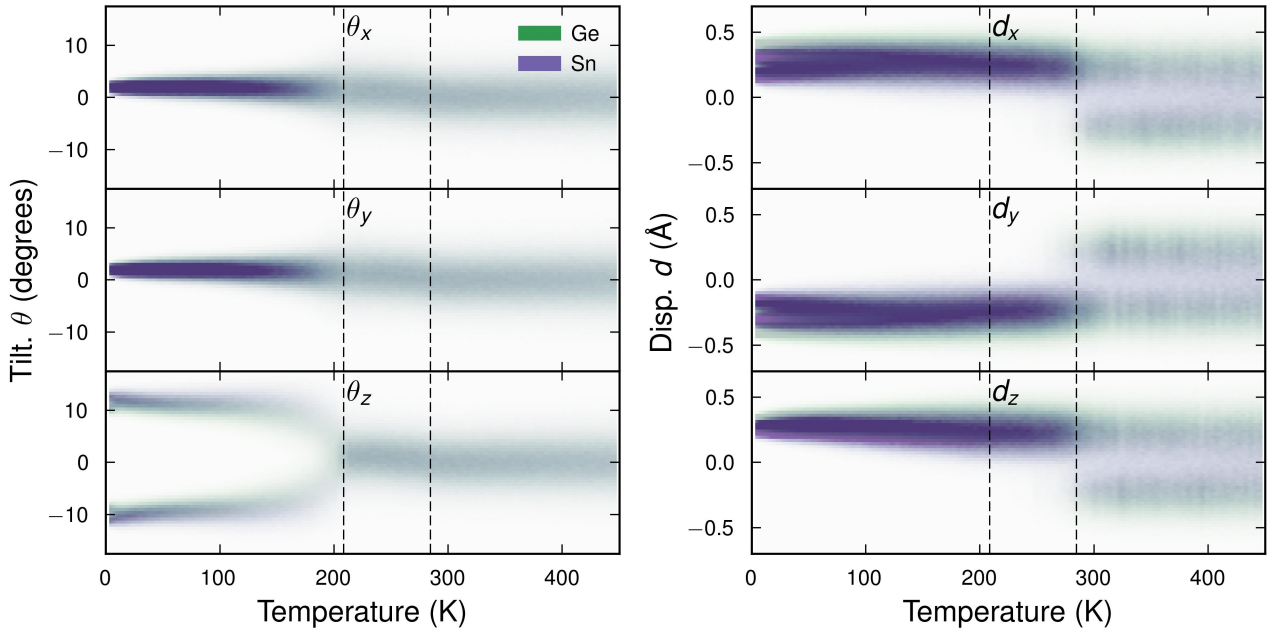

Figure S11: Temperature-dependent distributions of the octahedral tilt angles (θ; left) and B-site off-centering displacements (d; right) along the x, y, and z directions for $MAGe_{0.6}Sn_{0.4}I_3$, with the Ge and Sn distributions shown in green and purple, respectively. The vertical dashed lines denote the phase-transition temperatures.

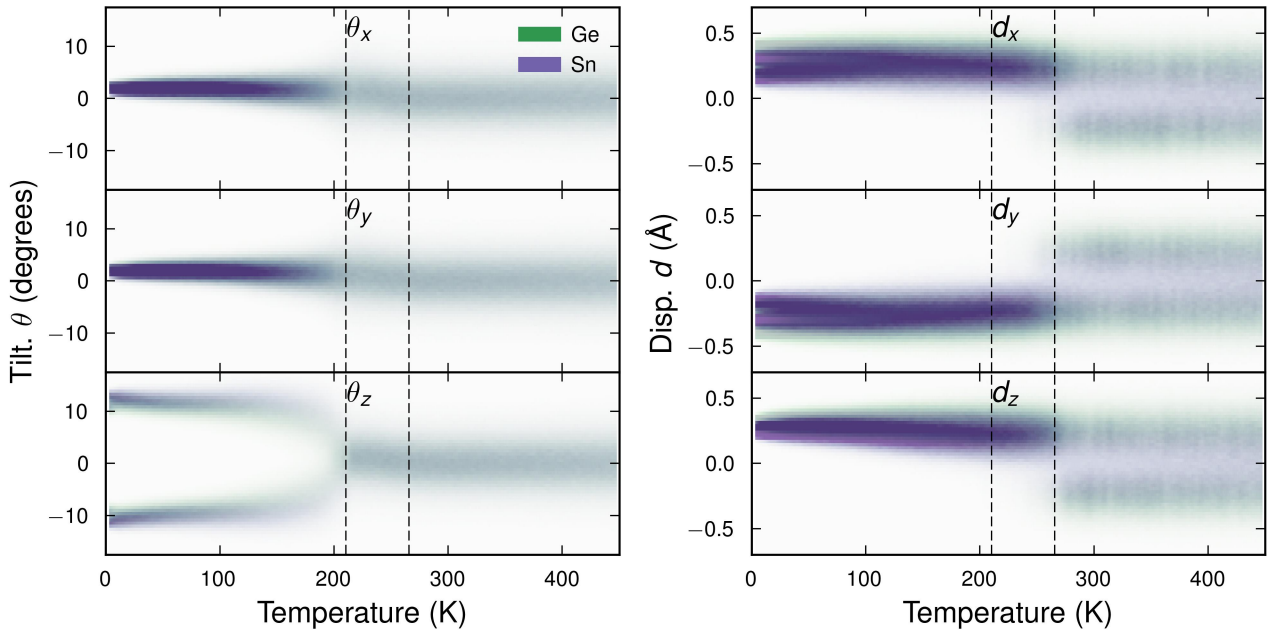

Figure S12: Temperature-dependent distributions of the octahedral tilt angles (θ; left) and B-site off-centering displacements (d; right) along the x, y, and z directions for $MAGe_{0.5}Sn_{0.5}I_3$, with the Ge and Sn distributions shown in green and purple, respectively. The vertical dashed lines denote the phase-transition temperatures.

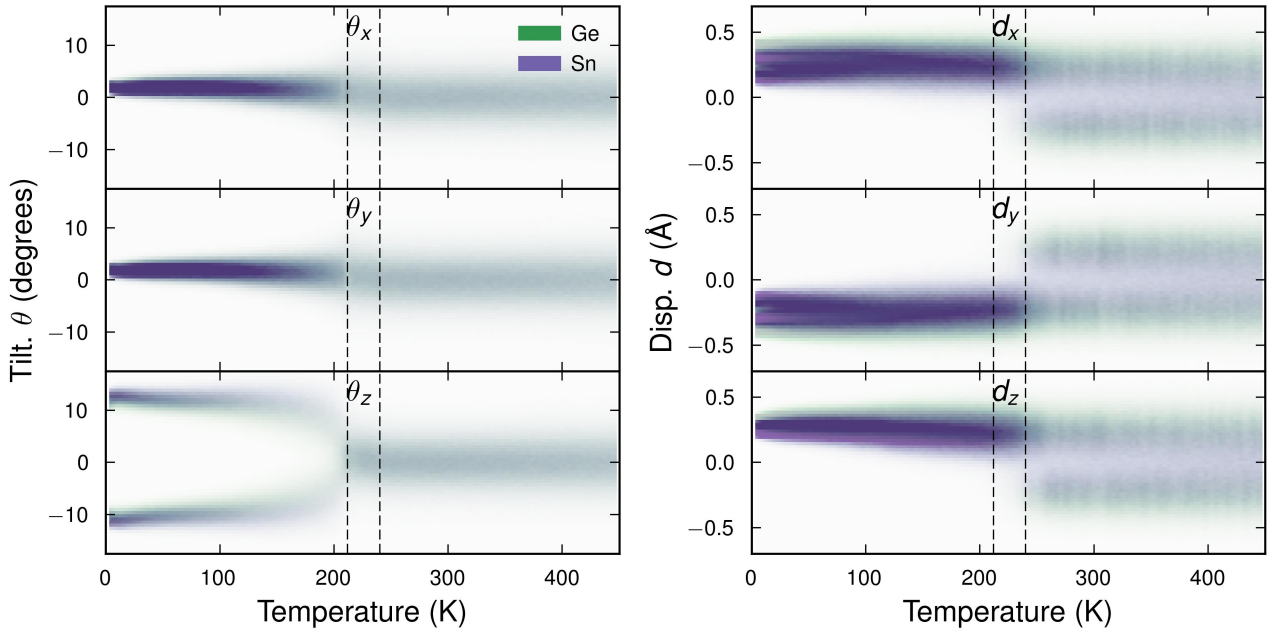

Figure S13: Temperature-dependent distributions of the octahedral tilt angles (θ; left) and B-site off-centering displacements (d; right) along the x, y, and z directions for $MAGe_{0.4}Sn_{0.6}I_3$, with the Ge and Sn distributions shown in green and purple, respectively. The vertical dashed lines denote the phase-transition temperatures.

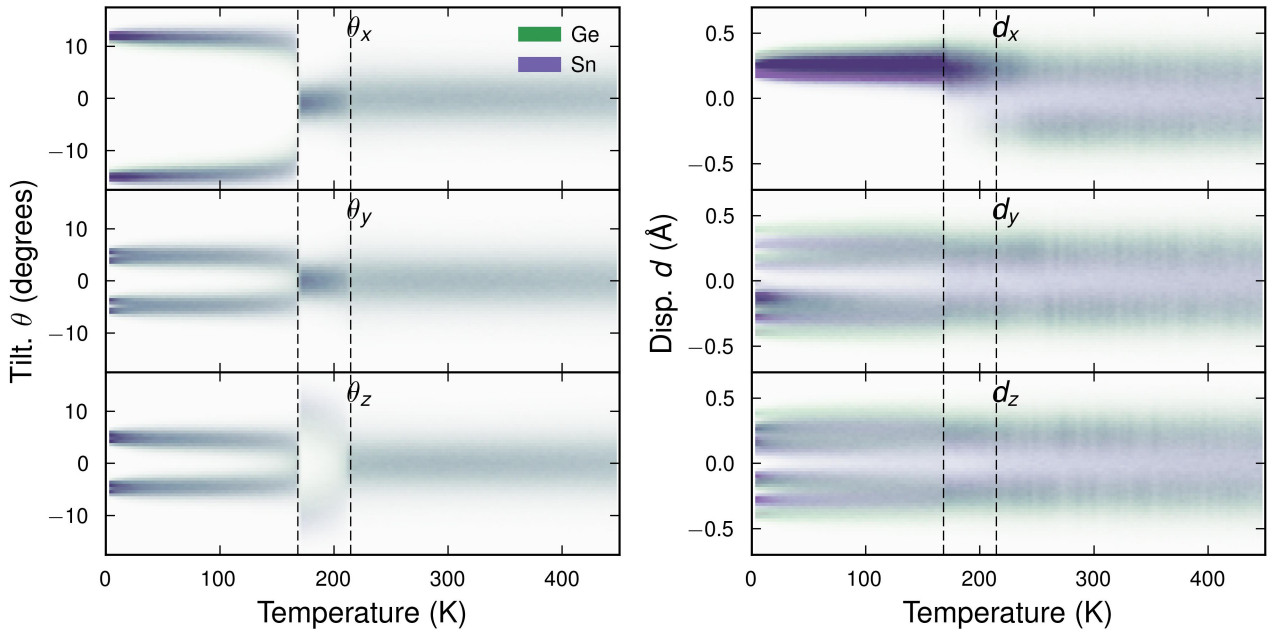

Figure S14: Temperature-dependent distributions of the octahedral tilt angles (θ; left) and B-site off-centering displacements (d; right) along the x, y, and z directions for $MAGe_{0.3}Sn_{0.7}I_3$, with the Ge and Sn distributions shown in green and purple, respectively. The vertical dashed lines denote the phase-transition temperatures.

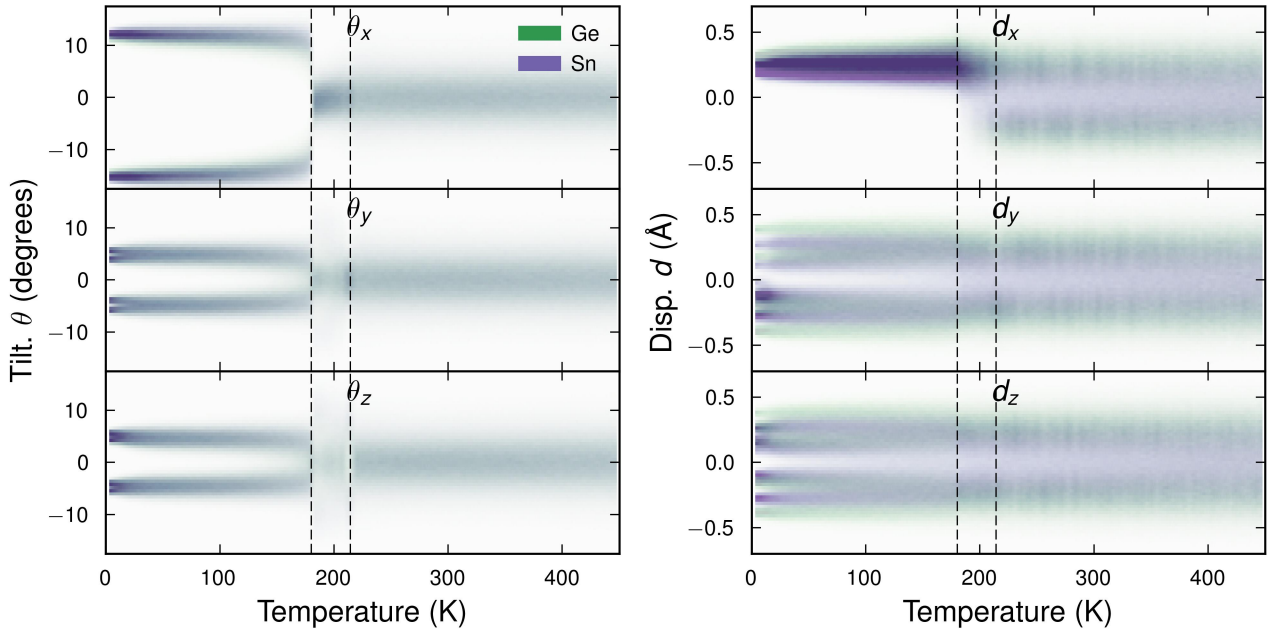

Figure S15: Temperature-dependent distributions of the octahedral tilt angles (θ; left) and B-site off-centering displacements (d; right) along the x, y, and z directions for $MAGe_{0.2}Sn_{0.8}I_3$, with the Ge and Sn distributions shown in green and purple, respectively. The vertical dashed lines denote the phase-transition temperatures.

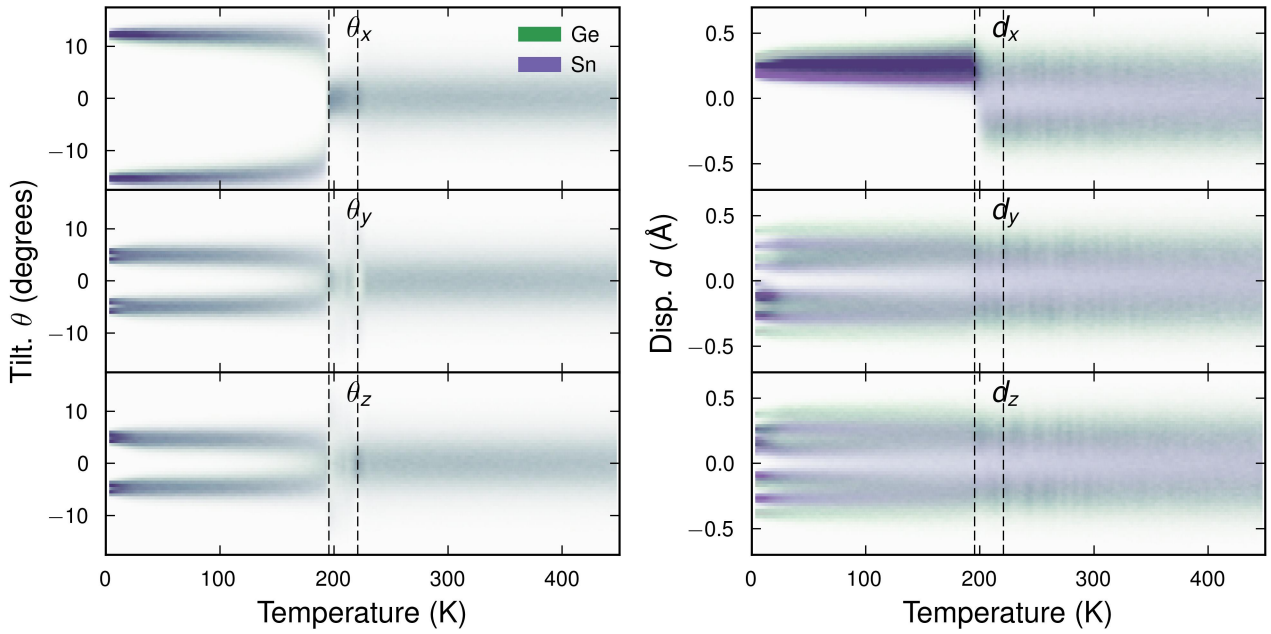

Figure S16: Temperature-dependent distributions of the octahedral tilt angles (θ; left) and B-site off-centering displacements (d; right) along the x, y, and z directions for $MAGe_{0.1}Sn_{0.9}I_3$, with the Ge and Sn distributions shown in green and purple, respectively. The vertical dashed lines denote the phase-transition temperatures.

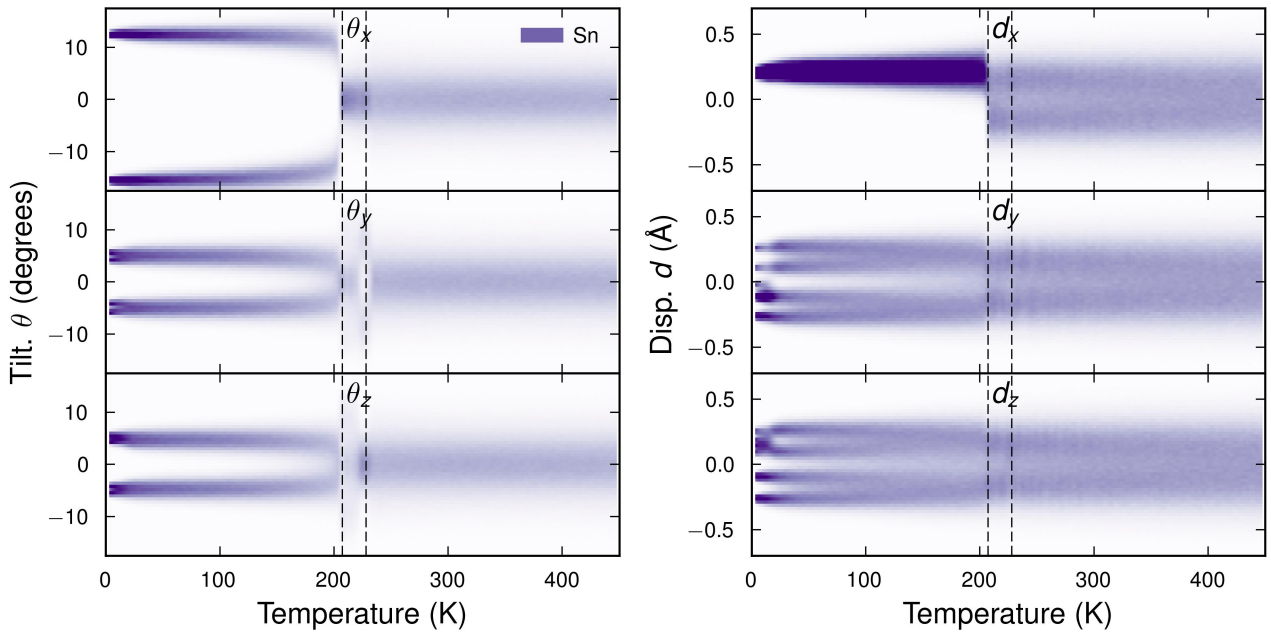

Figure S17: Temperature-dependent distributions of the octahedral tilt angles (θ; left) and B-site off-centering displacements (d; right) along the x, y, and z directions for $MASnI_3$, with the Sn distribution shown in purple. The vertical dashed lines denote the phase-transition temperatures.

Supplementary References

[S1] Blum, V.; Gehrke, R.; Hanke, F.; Havu, P.; Havu, V.; Ren, X.; Reuter, K.; Scheffler, M. Ab initio molecular simulations with numeric atom-centered orbitals. *Comput. Phys. Commun.* **2009**, *180*, 2175–2196.

[S2] Furness, J. W.; Kaplan, A. D.; Ning, J.; Perdew, J. P.; Sun, J. Accurate and Numerically Efficient r^2SCAN Meta-Generalized Gradient Approximation. *J. Phys. Chem. Lett.* **2020**, *11*, 8208–8215.

[S3] Bursch, M.; Neugebauer, H.; Ehlert, S.; Grimme, S. Dispersion corrected r^2SCAN based global hybrid functionals: r^2SCANh, r^2SCAN0, and r^2SCAN50. *J. Chem. Phys.* **2022**, *156*, 134105.

[S4] Fan, Z. et al. GPUMD: A package for constructing accurate machine-learned potentials and performing highly efficient atomistic simulations. *J. Chem. Phys.* **2022**, *157*, 114801.

[S5] Xu, K. et al. GPUMD 4.0: A high-performance molecular dynamics package for versatile materials simulations with machine-learned potentials. *Mater. Genome Eng. Adv.* **2025**, *3*, e70028.

[S6] Fan, Z. et al. qNEP: A Highly Efficient Neuroevolution Potential with Dynamic Charges for Large-Scale Atomistic Simulations. *J. Chem. Theory Comput.* **2026**, *22*, 4787–4801.

[S7] Ziegler, J. F.; Biersack, J. P.; Littmark, U. *The Stopping and Range of Ions in Matter*; Pergamon: New York, 1985; Vol. 1.

[S8] Liu, D.; Zeng, H.; Peng, H.; Sa, R. Computational study of the fundamental properties of Zr-based chalcogenide perovskites for optoelectronics. *Phys. Chem. Chem. Phys.* **2023**, *25*, 13755–13765.

[S9] Larsen, A. H. et al. The atomic simulation environment—a Python library for working with atoms. *J. Phys.: Condens. Matter* **2017**, *29*, 273002.

[S10] Lindgren, E.; Rahm, M.; Fransson, E.; Eriksson, F.; Österbacka, N.; Fan, Z.; Erhart, P. calorine: A Python package for constructing and sampling neuroevolution potential models. *J. Open Source Software* **2024**, *9*, 6264.